Vibration Analysis for Diamond Bremsstrahlung Targets

Christopher Pelletier

University of Connecticut

Storrs, CT 06269

christopher.d.pelletier@gmail.com

Advisor: Dr. Richard Jones, Department of Physics

Abstract

The atomic nucleus is made up of protons and neutrons, which are in turn comprised of quarks. The particles binding the quarks together are known as gluons. The way that quarks and gluons are assembled into physical states is still not entirely understood, specifically how they are confined in the nucleus such that lone quarks are never seen. The nuclear physics group at the University of Connecticut is part of the GlueX Experiment, which hopes to probe directly the gluon bond between quarks and understand its quantum mechanical properties. The probe used by GlueX is a high energy (small wavelength), polarized photon generated by a technique known as coherent bremsstrahlung. This technique involves radiation of photons as a high energy electron beam passes through a carefully oriented diamond wafer. To reduce unwanted background from electrons striking materials other than the diamond, it is necessary to suspend the diamond wafer on thin wires, rather than on a rigid mount. The design of the wire mount faces conflicting requirements of low mass and high stiffness so that the diamond orientation is precisely maintained. The goal of this project is to design a wire mount with minimum mass that meets the stability requirements for GlueX. An investigation was made into the prior existing design based on stretched tungsten wires, showing that this design did not meet the requirements. An alternate design based upon carbon fibers was developed and tested. The results obtained demonstrated a significant improvement over the prior design.

Contents

Table of Figures

1. Introduction

The Thomas Jefferson National Accelerator Facility located in Newport News, Virginia is a nuclear physics laboratory funded by the Department of Energy. Among the many projects being conducted at Jefferson Lab is the Gluonic Excitations Experiment (GlueX). The purpose of this experiment is to understand the properties of bound states of quarks and gluons (hadrons) in quantum chromodynamics (QCD), the governing theory behind the strong interactions. Hadrons come in two flavors, baryons and mesons. Baryons are bound states of three quarks, of which protons and neutrons are the best known, and mesons are bound states of a quark and an anti-quark. The role played by gluons in hadrons is to form the bonds which tie quarks together. These bonds are sometimes referred to as "flux tubes."

The GlueX collaboration seeks to gain a quantitative understanding of the principle of confinement, the binding of quarks within hadrons, by exciting the flux tube between the quark and anti-quark in a meson [1]. By doing this they will be forming a new type of matter known as a hybrid meson. These states have been postulated [2] and some experimental sightings have been reported, but no unambiguous identifications have yet been established. To accomplish this, researchers will use a highly polarized photon beam to probe the gluonic bond formed between quarks. Researchers will attempt to excite this bond to study its resonance characteristics.

To produce this photon beam, a process known as bremsstrahlung (German for "breaking radiation") will be used. High energy electrons will be passed through a thin diamond

wafer. As the electrons interact with the atoms in the diamond they lose energy in the form of electromagnetic radiation. Because bremsstrahlung occurs when the electrons interact with any matter, it is necessary to suspend the diamond wafer, so as to prevent interactions of the electron beam with the target mount. In order to control the polarization of this photon beam the diamond must be suspended in such a way that vibrations are severally restricted. It is the goal of this research project to develop a technique for analyzing that vibration and to develop an appropriate mounting technique which reduces vibration below maximum permissible levels. There is an intrinsic beam divergence of 15 μrad due to the beam emittance. The mounting will need to ensure that the diamond vibration amplitude is below this specification.

2. Background Information

2.1 Particle physics of strong interactions

All matter is comprised of atoms. These atoms are comprised of small particles known as protons, neutrons, and electrons. From the time of the discovery of the electron by J.J. Thompson in 1897 [3] to the discovery of the atomic nucleus by Ernest Rutherford in 1911 [4] until the 1960's, it was believed that protons and neutrons were elementary particles, that they could not be subdivided. Then, in 1964, two scientists, Murray Gell-Mann and George Zweig, independently proposed the quark model. Both scientists proposed that protons and neutrons were composed of quarks and anti-quarks, as depicted in Fig. 1 [5][6]. These original models identified three flavors of quarks, today called the up quark, the down quark, and the strange quark. Later research by Sheldon Lee Glashow and James Bjorkin in 1965 and Makoto Kobayashi and Toshihide Maskawa in 1970 yielded the discovery of three more quarks, the charm quark, the top quark, and the bottom quark.

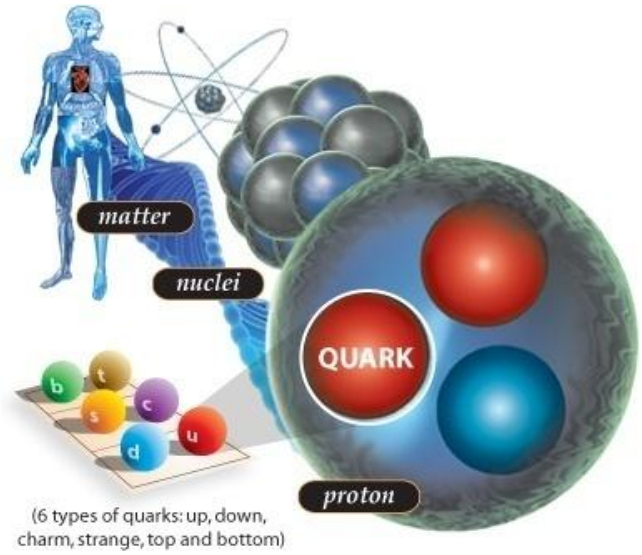

Figure 1: The composition of matter

Quarks interact with each other through the strong force. The particle which mediates this force is known as a gluon. Unlike the electromagnetic force which decreases in strength when the distances between the two charges increase, the strong force is asymptotically constant at large distance. This principle is known as confinement. When scientists attempt to separate quarks, in a meson for instance, the energy applied to the system is sufficient to spontaneously create two new quarks, leading to two mesons, as opposed to two free quarks. In order to quantify the coupling between quarks and gluons via the strong force scientists coined the term "color charge."

2.1.1 Bound States of Quarks and Gluons

The principle of confinement makes use of a property of particles known as color charge. Quarks take on one of three colors, red, blue, and green, and anti-quarks can take on

one of three, anti-colors, anti-red, anti-blue, and anti-green [7]. Gluons carry both a unit of color and one unit of anti-color charge. QCD demands that all hadrons are color-neutral. One consequence of this is that baryons, protons for instance, must be made of three quarks each, with a different color. Mesons, a quark/anti-quark pair, must have one quark with one color and the other with the corresponding anti-color. When gluons are exchanged between quarks, the colors of these quarks change, but the end product must always be color neutral.

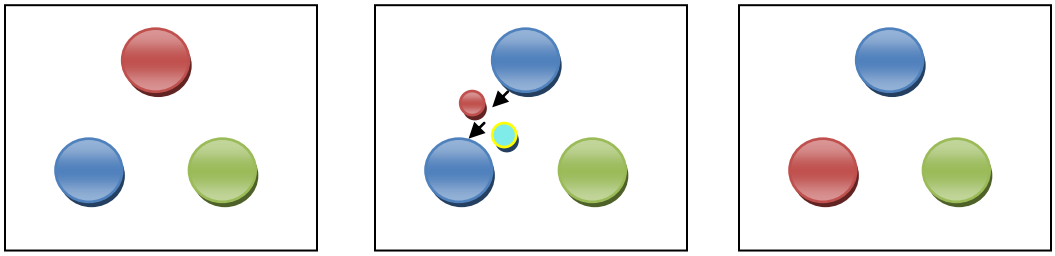

Figure 2: The conservation of color charge in gluon exchange. The cartoon proceeds from left to right.

In Fig. 2 the red and blue quarks interact when the red quark emits a red, anti-blue gluon. The end result is that the color of the red quark is now blue and the blue quark is now red, conserving the color neutrality. Unlike quarks, gluons are electromagnetic charge-neutral, meaning that they cannot be detected using electromagnetic probes, such as electron microscopy. Researchers must develop other techniques in order to image these gluons. One way to detect their presence would be to excite the flux tubes binding the quarks in normal mode oscillations and measure their resonance spectrum.

2.2 GlueX Experiment

2.2.1 Beam Line

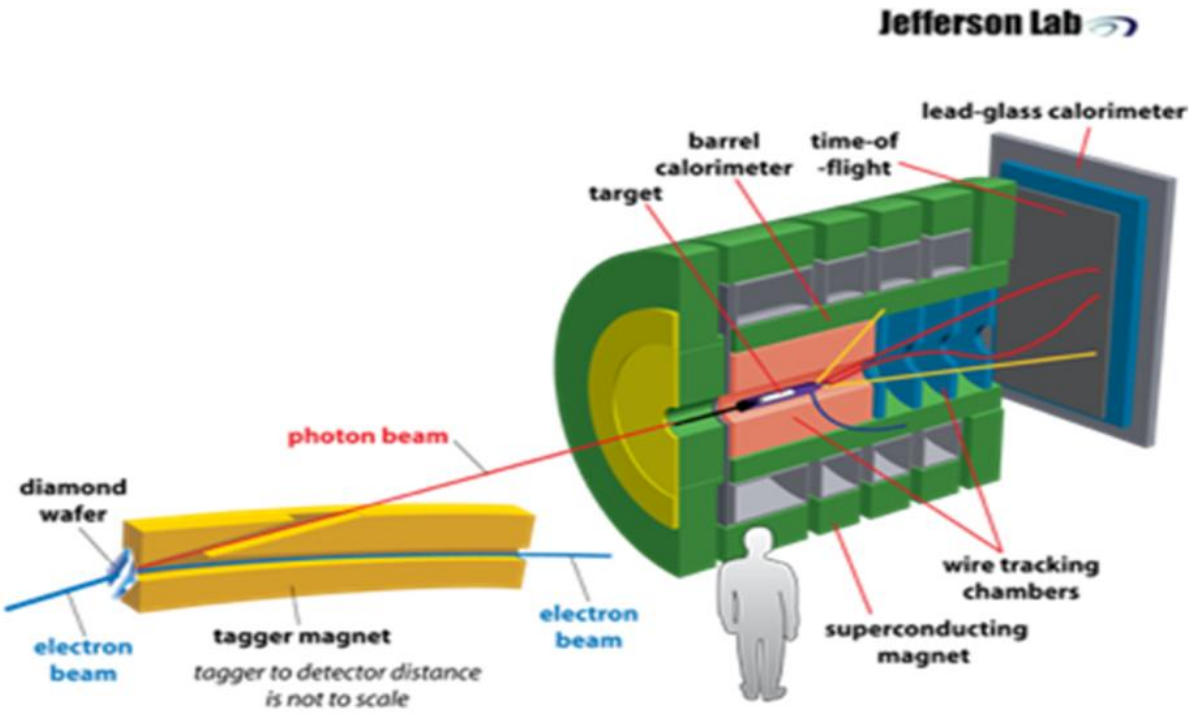

Figure 3: Overview of the GlueX experiment

In order to produce the high energy electrons necessary to perform this experiment, GlueX researchers will use a 12GeV electron accelerator located at Jefferson Lab. The electrons will pass through six passes of the accelerator, gaining 2GeV each pass. As shown in Fig. 3, once the electron beam leaves the accelerator it passes through a diamond wafer, producing a photon beam. These photons will collide with a liquid hydrogen target producing mesons of all types. The various instruments pictured in the figure are used to detect the hybrid meson states which researchers are attempting to find.

2.2.2 Beam Properties

The electron beam from the accelerator has an intrinsic beam divergence Δα that depends upon the transverse size Δx of the beam. The Heisenberg uncertainty principle places a lower limit on this divergence,

$$\Delta x \, \Delta \alpha \geq \frac{\hbar}{2p} \qquad (1)$$

where *p* is the momentum of the beam. This limit is very small. For the total length of travel L of an electron in the JLab accelerator (8400m), the divergence due to the uncertainty principle leads to a transverse beam expansion factor of only $1+2.45\times10^{-11}$ for a beam of radius $\Delta x=10^{-4}$m. The product $\Delta x \, \Delta \alpha$ shown in Eq. 1 is known in accelerator physics jargon as the "beam emittance." The minimum emittance required by the Heisenberg uncertainty principle assumes that the electrons are emitted from an absolute zero temperature source. In fact, the source temperature is far above absolute zero, and contributes most of the emittance of the beam from the JLab accelerator at energies below 6GeV.

For the 12GeV electron beam at JLab, the beam emittance growth during acceleration comes mainly from two sources, synchrotron radiation and optical aberrations in the magnetic field of the beam line magnets. Synchrotron radiation refers to the acceleration the electrons encounter when moving through the curved sections of the accelerator. As they are accelerated through the curved path the electrons experience acceleration and emit photons.

The momentum recoil of these emitted photons “kicks” the electrons in both transverse and longitudinal directions, broadening its divergence, and increasing its energy spread.

There is one final effect which contributes to the overall beam divergence, chromatic optical aberrations. This effect is seen when electrons in the beam are slightly off axis. Again, there is a “kick”, this time by the quadrapole magnets that maintain the beam’s focus. The kick angle, as given by Chao [9], is

$$\Delta x' = K_0 x \frac{1}{1+\delta} \rightarrow \Delta x' = K_0 x(1 - \delta + \delta^2 - \cdots) \qquad (2)$$

where K_0 is the quadrapole gradient and δ is the uncertainty in energy of the off-axis electron. For large magnetic fields this can be significant. In order to reduce these effects sextupole magnets can be installed, which reduce the chromatic aberrations but introduce other non-linear effects in the horizontal electron position. As mentioned previously for the 12GeV beamline at JLab, the total beam divergence in the horizontal direction at the position of the photon radiator will be $\Delta\alpha \approx 15\mu rad$.

3. Diamond vibration

3.1 Mechanical vibration

Every system has some frequency at which it vibrates, called its natural frequency. Natural frequency is a consequence of the mechanical characteristics of the system. Each system will have a fundamental natural frequency for each degree of freedom. Typically only the lowest order vibrations are important. When a system is driven at one of its natural frequency the vibrational amplitude begins to increase. It is important to have a firm understanding of the vibrational characteristics of our diamond mount system because we want to keep amplitude of vibration as low as possible. Background vibration from other systems present near the diamond mount could potentially drive the vibration amplitude up. For instance many mechanical components, generators for instance, vibrate at exactly 60Hz. If our diamond system were to have a natural frequency at or near 60Hz it would be disastrous for the photon production. The reason for this is that the energy of the photons emitted in the process of coherent bremsstrahlung is sensitive to the angle between the incident electron beam direction and the unit normal to the crystal planes. Any deviation in this angle from the desired setting by more than the beam divergence degrades the polarization of the photon

beam, as shown in Fig. 4.

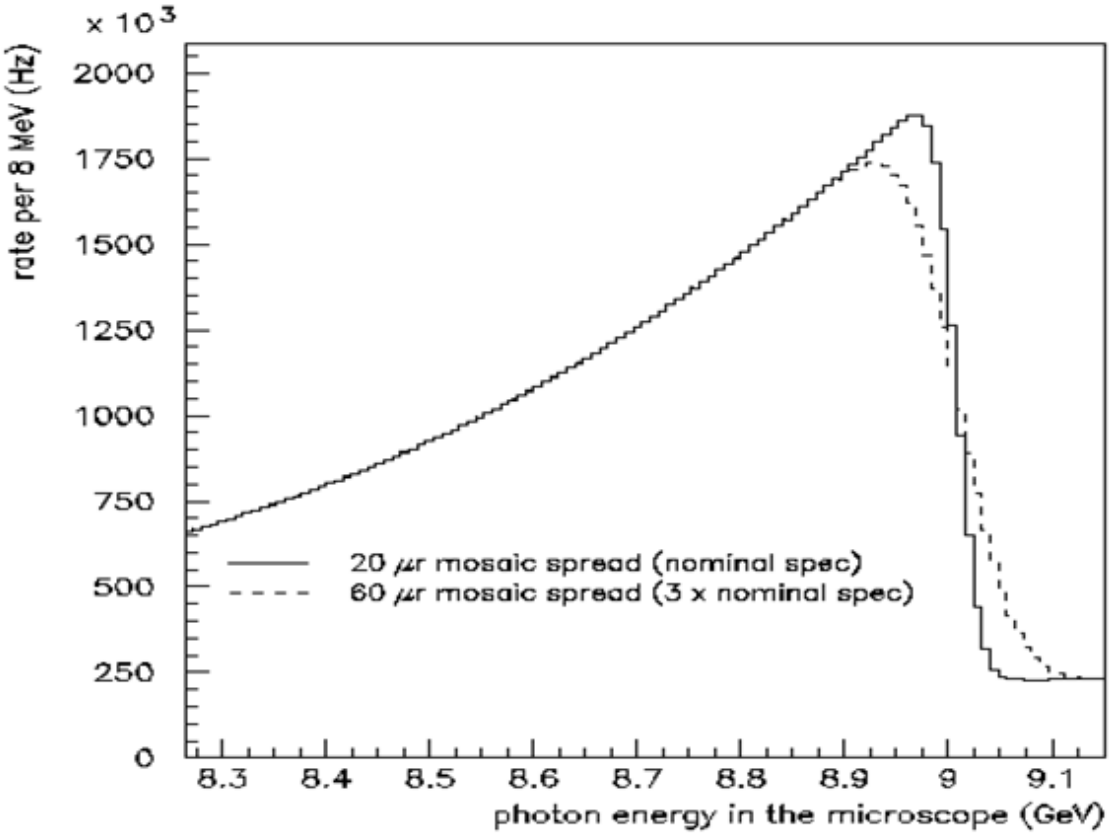

Figure 4: Degradation of photon polarization due to mechanical vibration above the specification based on beam divergence

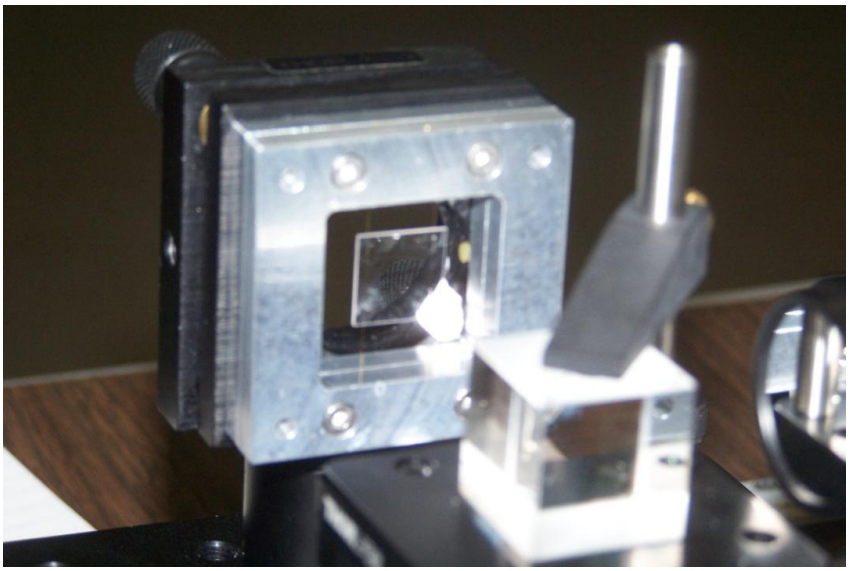

Figure 5: Geometry of the diamond mount system

We can determine the theoretical natural frequency by looking at the geometry of the mount system. As shown in Fig. 5 the diamond is mounted on two fibers strung vertically. These fibers have some intrinsic vibrational characteristics as does the system of the diamond mounted on these fibers. Given a wire length w and an applied wire tension F_T the frequency of vibration about the y axis, for instance, can be found to be

$$\omega^2 = \frac{4\omega F_T \cot\left(\frac{w\omega}{v}\right)}{vm} \tag{3}$$

where m is the system mass and v is the speed of a wave traveling on the wires

$$v = \sqrt{\frac{F_T}{\frac{m_{wire}}{w}}} \tag{4}$$

A detailed discussion of this procedure can be seen in a later section.

3.2 Effect on the rocking curve

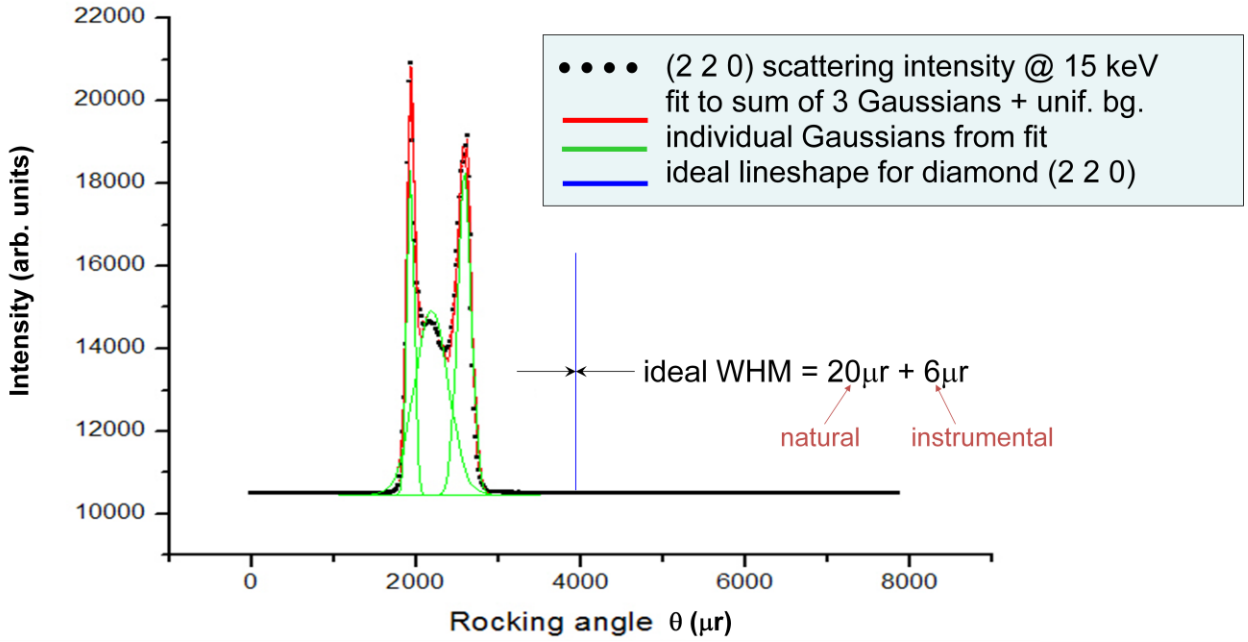

Figure 5: Intensity of X-ray diffraction versus rocking angle

During the fall of 2009, the first commercially produced diamond which met our thickness specifications were produced. In an effort to determine the planarity of these diamonds, the first diamond mount was constructed. This mount was brought to the Cornell High Energy Synchrotron Source (CHESS) to analyze the diamonds rocking curve. When the initial mount was constructed it was thought that the tension applied to the mount would be sufficient to maintain the diamond in a stable position. The mosaic spread of the crystal was determined to be 20μrad and the thought at the time was that the instrumentation would add another 6μrad divergence. Given these two divergence parameters the ideal lineshape for the diamond was produced, shown in blue. When the rocking curve data was taken, however, there was significantly larger width than expected for the rocking curve. Initially it was believed

that the crystal warping was the major contributor to the width of the rocking curve. After further analysis, however, it was determined that mechanical vibration was the most significant contribution to the spread in rocking curve.

3.3 Increasing vibrational frequency

As discussed earlier the vibrational frequency of the first mount was too low to allow for stability of the diamond within the 15μr specification. Going back to Eq. 3, it can be shown that there are two parameters of the mount which can be changed in order to increase vibrational frequency. To a first order approximation the equation for ω can be rewritten as:

$$\omega^2 = \frac{4\omega F_T \cot\left(\frac{w\omega}{v}\right)}{vm} \approx \frac{4\omega F_T \frac{v}{w\omega}}{vm} \qquad (5)$$

$$\omega^2 = \frac{4F_T}{Wm} \Rightarrow \omega = 2\sqrt{\frac{F_T}{Wm}} \qquad (6)$$

By rewriting the equation in this way it is easy to see that the two parameters which are tunable are the applied tension F_T and the wire length W. By increasing the applied tension and/or decreasing the wire length the vibration frequency will increase. The vibration amplitude is directly dependent on the modes of background noise. In particular power production in the United States has an AC frequency of 60Hz, meaning many electrical components (generators for instance) run at 60Hz. The amplitude of background noise around

this frequency high compared to other frequencies, so it is desirable to be well above this frequency.

3.4 Measuring vibration using interferometry

Before the end of the 19th century there was a commonly held belief that there was a luminiferous aether through which light propagated. In 1887, Albert Michelson and Edward Morley sought to quantify the effects that the "aether winds," the supposed consequence of the earth moving rapidly through this aether, had on the speed of light. [8] The results of their experiment were inconclusive. They failed to find the shift in aether winds they were looking for, but out of this "failed" experiment came a very accurate device by which small changes in position can be detected.

The interferometer uses a principle known as superposition in order to allow for the detection of very small changes in position. Superposition states that the displacement due to a wave at any point is the vector sum of different waves acting at that point. For instance, if two waves are acting with the same amplitude at the same location and one is at peak amplitude while the other is a trough, these waves will destructively interfere, resulting in a zero amplitude wave at the point in question. If instead both wave fronts were at their peak, the waves would interfere constructively, leading to a wave which is twice as large as the original two waves.

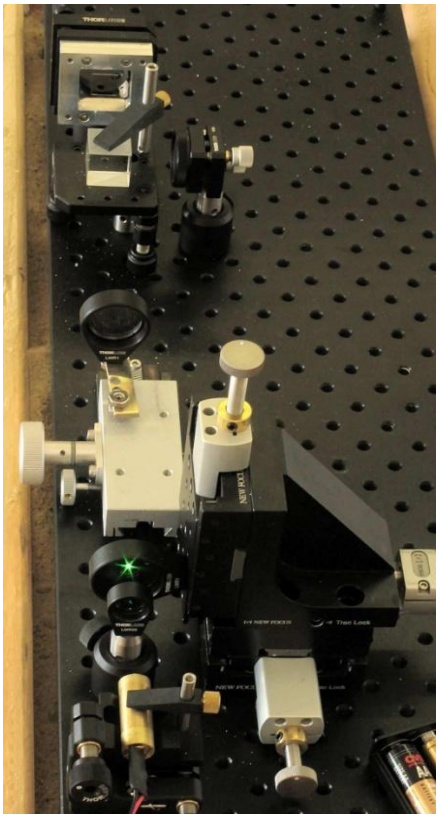

Figure 6: Michelson interferometer used in our experiment

The interferometer uses a coherent light source to make measurements on a sample. The beam passes through a pin hole, which removes spherical aberrations and expands the beam. It also causes the beam to become highly divergent. Once the beam is expanded it is passed through a plano-convex lens in order to return the beam to parallel.

When light is passed through a small opening a phenomenon known as diffraction occurs. Diffraction is a result of the interference caused by different parts of the wave front being different lengths from a reference surface. As a result some of the waveform is slightly shifted, causing destructive interference. When light is passed through a pin hole, the pattern which is formed is known as an Airy Pattern. Because the end result is to use a coherent beam to perform the Interferometry it is necessary to remove the fringe patterns. As a consequence,

the diameter and focal length of the converging mirror need to be chosen so that the lens is illuminated by only the central maxima. (A complete analysis of the Airy pattern and its consequences on converging lens choice can be found in Appendix A.2) In particular, for the 5μm pinhole which is used in this experiment it is necessary to have a converging lens with a focal length of f=200mm.

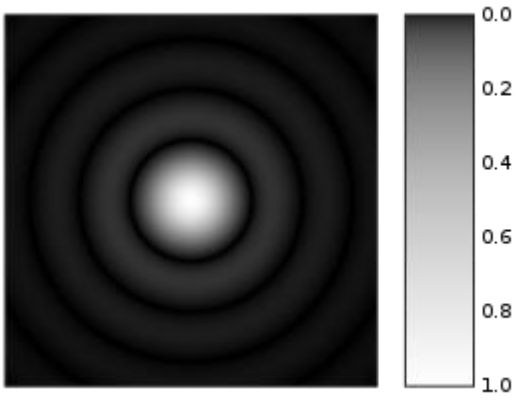

Figure 7: Computer image of an Airy Pattern

Once the light is expanded and returned to parallel it is passed through beam splitter cube. This splits the beam into two equal parts. One part passes through the mirror while the other is reflected. One of these parts travels to an optically flat mirror and is then reflected back to the cube. The other part travels to the sample we are trying to test. Again this beam is reflected off of the test surface and back into the cube. Once the two beam halves return to the cube they are recombined and reflected to a detector.

When these beams recombine they will interfere. If the two surfaces separated by an integer number of wavelengths of the source light there will be constructive interference. If they are a half integer separated there will be destructive interference. Because the test surface is not optically flat there will be some section with constructive interference and some

with destructive. This allows for the detection of surface features as small as the wavelength of the light source, 532nm in this case.

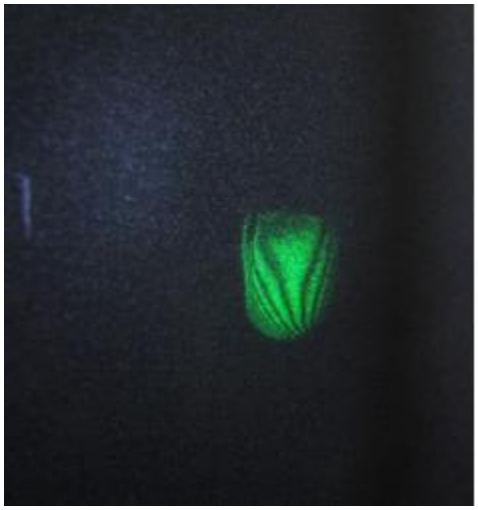

Figure 6: Interference pattern produced by reflections from a stretched Mylar sheet using the Michelson Interferometer

3.5 Decomposition into normal modes

In order to analyze the frequency of vibration of a system a technique known as a Fourier transform is performed. In essence the Fourier transform takes a data set which is in time space and converts it into a function in frequency space. It is commonly written as

$$f(x) = \int_{-\infty}^{\infty} f(\xi) e^{2\pi i x \xi} d\xi \qquad (7)$$

where $f(x)$ is the function in time space and $f(\xi)$ is its corresponding frequency components. Fourier transformations are used in this experiment to extract the natural frequency of the diamond vibration.

4. Development of an Imaging Technique for Vibration Analysis

4.1 Direct Imaging

If either the sample or the reference mirror is moving there is a shift in the recorded interference pattern. This shift can be measured to determine the frequency of vibration. Because of the high levels of vibration in the original diamond mounting scheme, Interferometry proved to be a difficult task in regards to determining vibrational frequency. In order to analyze the vibration a different technique needed to be developed. This technique is known as a direct imaging technique. A laser beam is shone off of the surface of the sample and the reflected spot is then sent to a detector. As the plane of the diamond rotates, so does the position of the reflected spot on the detector. This vibration can be analyzed in order to determine the vibration frequency of the diamond in the mount.

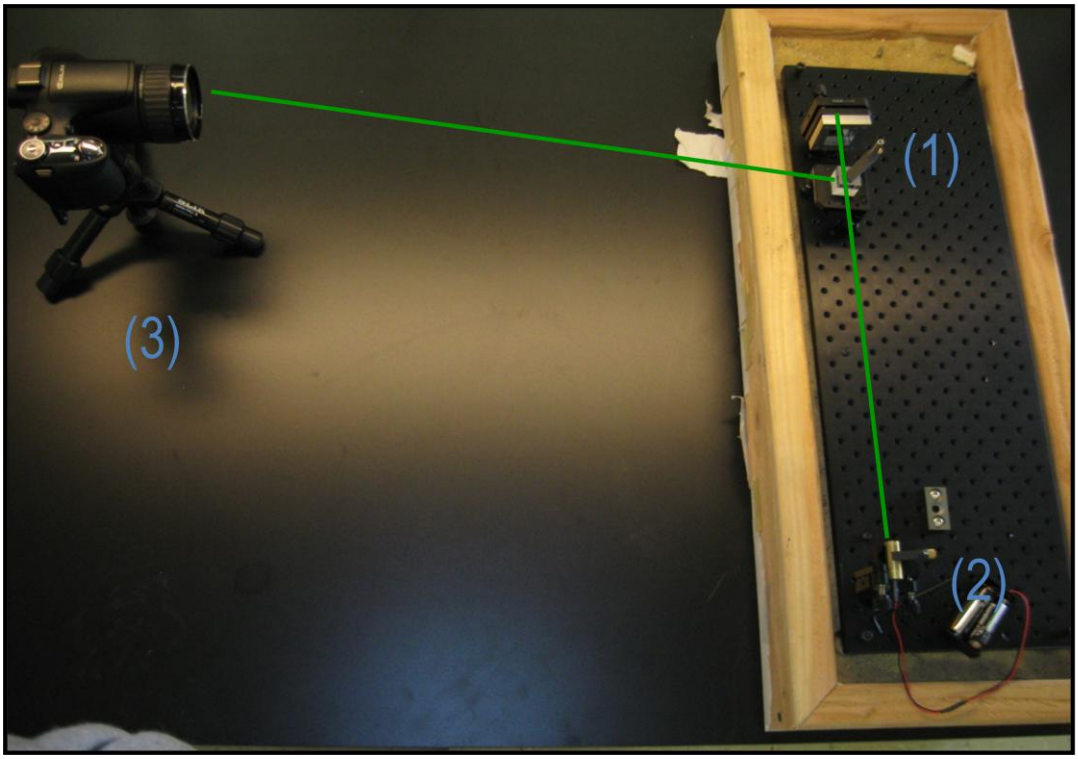

Figure 7: Direct imaging setup with diamond radiator (1), laser (2) and digital camera (3)

4.1.1 Lens Flare

Whenever a bright light is imaged across a comparably dark background an artifact known as a lens flare can be seen in the captured images from the camera. Typically these artifacts are undesirable. In this case, however, it was discovered that the lens flare had a very predictable behavior. As the lens flare moves along the front of the camera lens, the spot also moves relative to the CCD sensor in the camera, producing an set of images with varying lens flare position. The position is then analyzed to determine the vibration frequency. Also, after careful calibration it was possible to determine vibration amplitude based on the flare spot position relative to the mean spot position.

4.1.2 Calibration

In order to determine both the amplitude and frequency from a single video it was necessary to determine how the lens geometry mapped the lens flare position change on the image as a function of change in incident angle of the reflected spot from the sample surface. To do this the camera was set up on a 1.4m long rail which was fixed on one end and attached to a 1-d linear translation stage on the other. On the fixed end a mirror was mounted and the camera was mounted on the mobile end. A laser beam was reflected off of the mounted mirror and onto the surface of the camera lens. The camera position was changed in .5mm increments and the change in position of the lens flare was recorded for each movement.

It was expected that because of the shape of the lenses, there would be a greater change in the lens position for each movement on the outer edges and the movement would decrease the closer the flair spot got to the edges. What was found was that over the operation range, the realistic area which the moving flair spot sweeps out, the mapping is linear. Once this result was obtained a sweep of the usable area was done, stepping the camera .5mm and recording the resulting change in flare spot location. From this data a conversion factor was produced which equates a change in number of pixels into a rotation of the diamond surface in mrad. The calibration found that for a beam splitter to camera length of 1.4m there is a change of 23.55 pixels/mm or 32.975pixels/mrad. In order to measure a change in the direction of the normal vector to the diamond plane there must be a change in lens flare position of at least 2 pixels. The consequence of this that that the smallest divergence which can be recorded using the direct imaging technique is

$$\Delta_{min} = \frac{2\ pixels}{32.975 \frac{pixels}{mrad}} = .0607mrad = 60.7\mu rad \quad (8)$$

In order to image a 15µrad divergence using the direct imaging technique it would be necessary to have a minimum beam splitter to camera length of x=

$$\tan(15\mu rad) = \left(\frac{2pixels}{23.55 \frac{pixels}{mm}}\right) * \frac{1}{x} \quad (9)$$

$$x = 5661mm = 5.661m \quad (10)$$

This is the minimum length assuming a lens flare with high enough contrast to be able to distinguish changes in 1 pixel. In reality this would be significantly larger, on the order of $15m+$. This analysis shows that given the space constraints of the lab space it will be necessary to use interference techniques in order to image the change in the direction of the diamond plane below 60µrad.

4.2 Video Analysis

As mentioned previously there are two spots which are seen on the video frames. The first is the point to point focus of the beam spot. The second, fainter spot is the lens flare recorded by the camera. As the angle of the sample relative to the line of the beam changes the location of the flare spot also changes. In order to find the vibration characteristics the location of the flare spot for each frame needed to be located. A Matlab code was written by Igor Senderovich in order to perform the iterative process of finding the position of the flare spot in each frame. (The code used in this iterative process can be found in Appendix A.3). When the laser spot leaves the pinhole it is in the shape of a Gaussian. Even with the convolution which occurs when light passes through the camera lens system, it is assumed that the lens flare will also take on this shape.

The laser which is used in this interferometer is a 532nm 5mW green diode laser. Because the lens flare is produced from green light, the only channel with significant gain is the green channel. This channel is selected out and is made into a false color intensity graph. A fit function is invoked which compares the intensity of each pixel with the ideal peak intensity for a Gaussian with particular user defined characteristics. The program then defines the central location of the lens flare as the point with the smallest difference between the ideal intensity and the actual intensity. Because the point to point focus spot is significantly more intense than the lens flare the fit would tend to find the peak value for the Gaussian in this region. To prevent this issue from happening, the point to point focus is artificially blocked from these images via a mask.

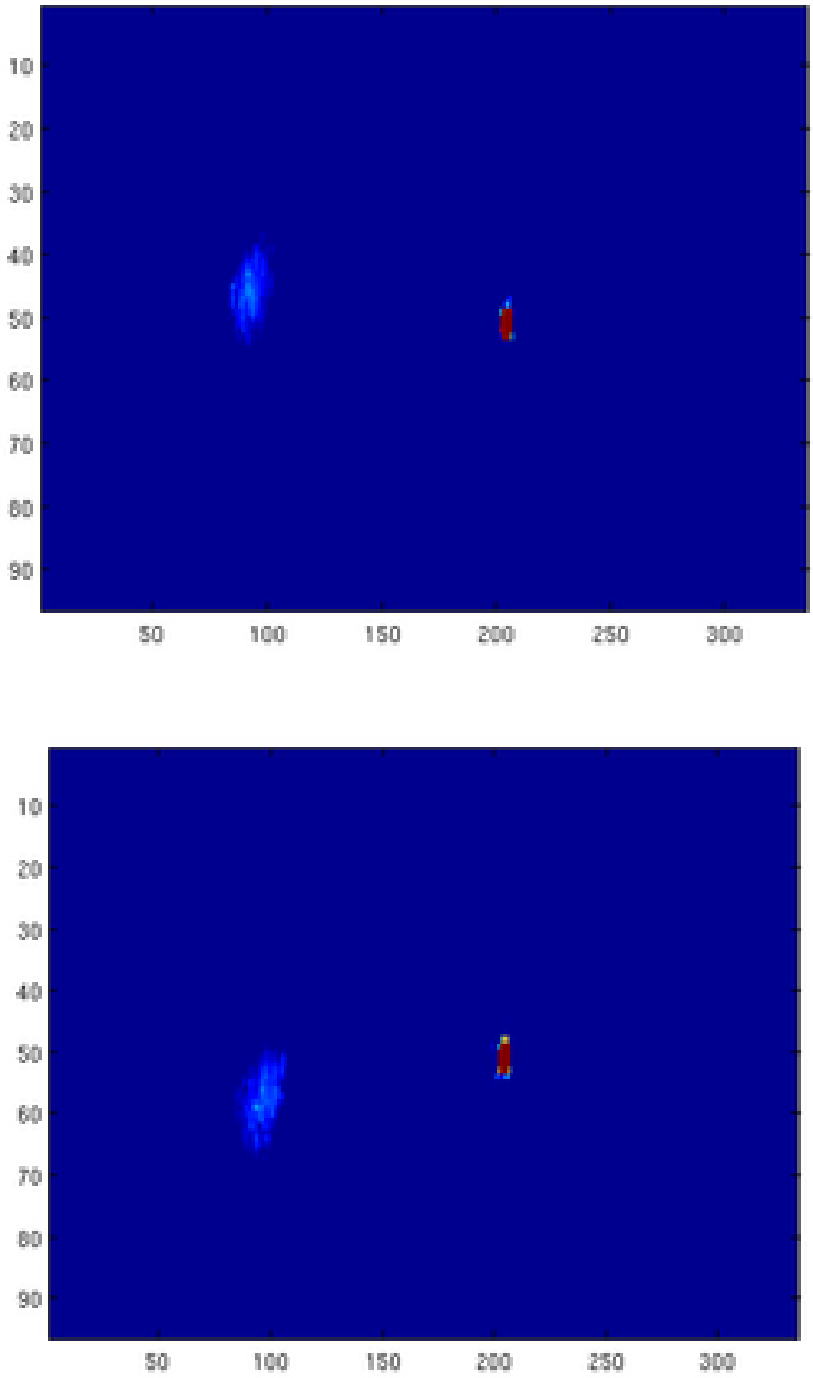

Figure 8: False color images of the lens flare as it moves relative to the camera sensor

The original intention was to use this code to process video but was ultimately found too slow for effective processing. An open source program, Tracker 4.00 by Dr. Douglas Brown of Cabrillo College, was ultimately used for video processing because of its speed and ease of use. This program tracks a user defined object as it moves throughout the video. The program assumes that the acceleration of the object is small from frame to frame, and uses a small search area around the object location from the previous frame in order to locate the object. This small search area leads to faster video processing times. Once the videos were processed, the changes in x and y position versus time were plotted. The data was then replotted using the conversion factor determined in the calibration to give a plot of angular displacement versus time.

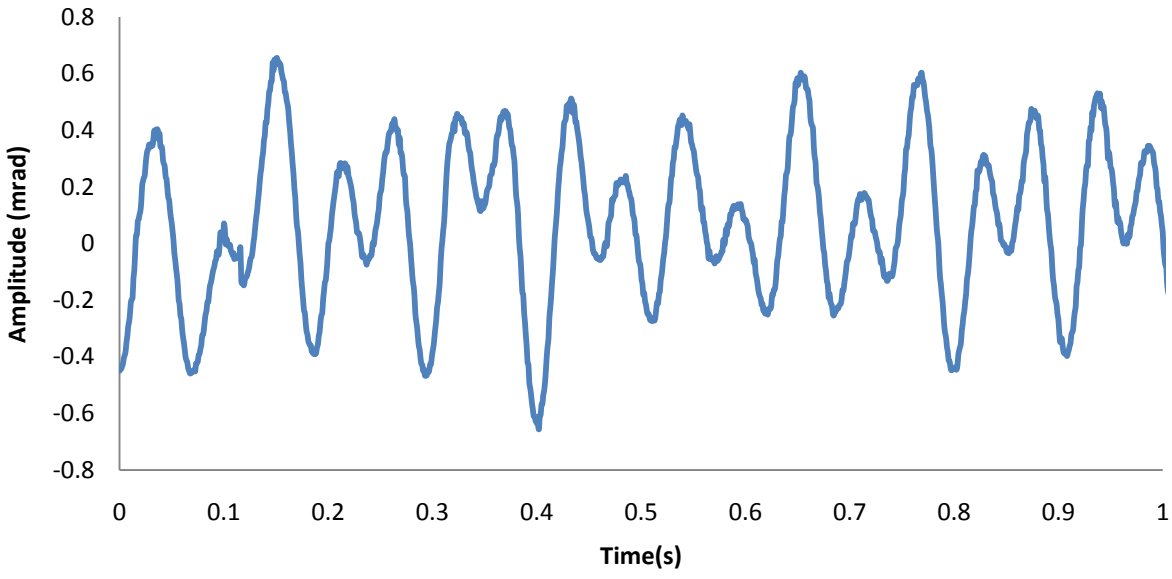

Figure 9: Rotation of diamond about y axis for original mount design

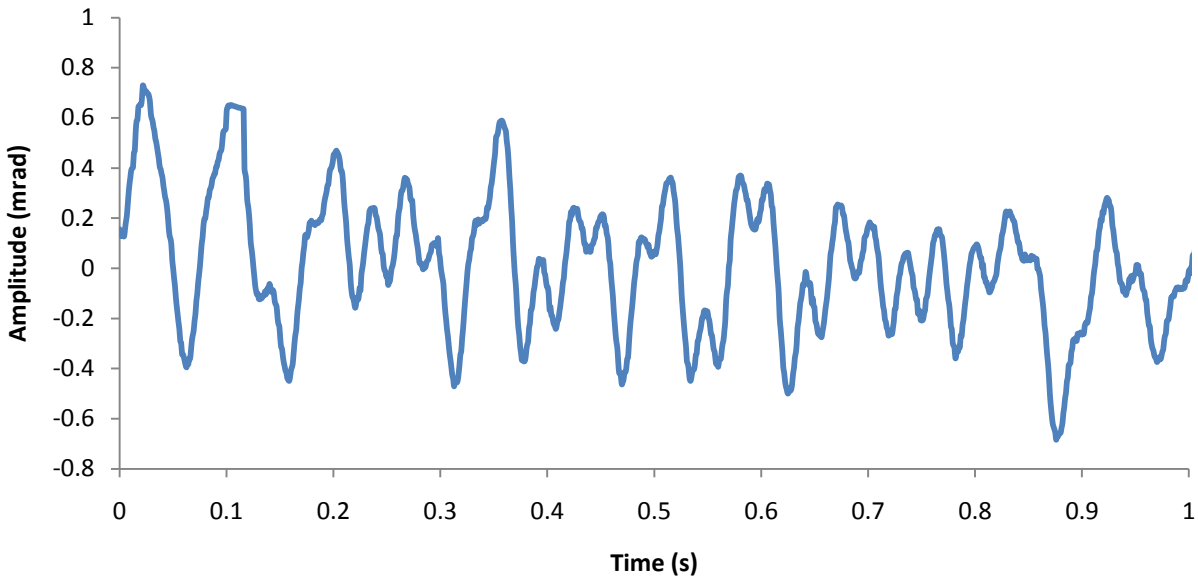

Figures 10: Rotation about the x axis for initial mount design

These two figures are for the initial mount design which Igor Senderovich had constructed several months prior to the beginning of this project. Analysis of these spectrums yields several interesting results. Most importantly, the frequency of the vibration was analyzed in order to determine if the mount was adequately holding the wire tension.

4.3 Determining Vibration Frequency

As mentioned previously a Fourier analysis is used to extract the frequency data from the position versus time graphs. There is a built in function in excel which allows for this type of analysis to be done. By analyzing the frequency spectrum and comparing it to the derived frequency it can be determined if the mount is sufficiently holding the wire tension. Again, the first order approximation for the fundamental frequency is found using Eq. 6. For this initial mount both of the wires were tensioned using the same weight and the total applied tension

for both wires was 5g. This gives a calculated fundamental frequency of f=22.28Hz. The Fourier spectrum was analyzed and the following spectrum was seen:

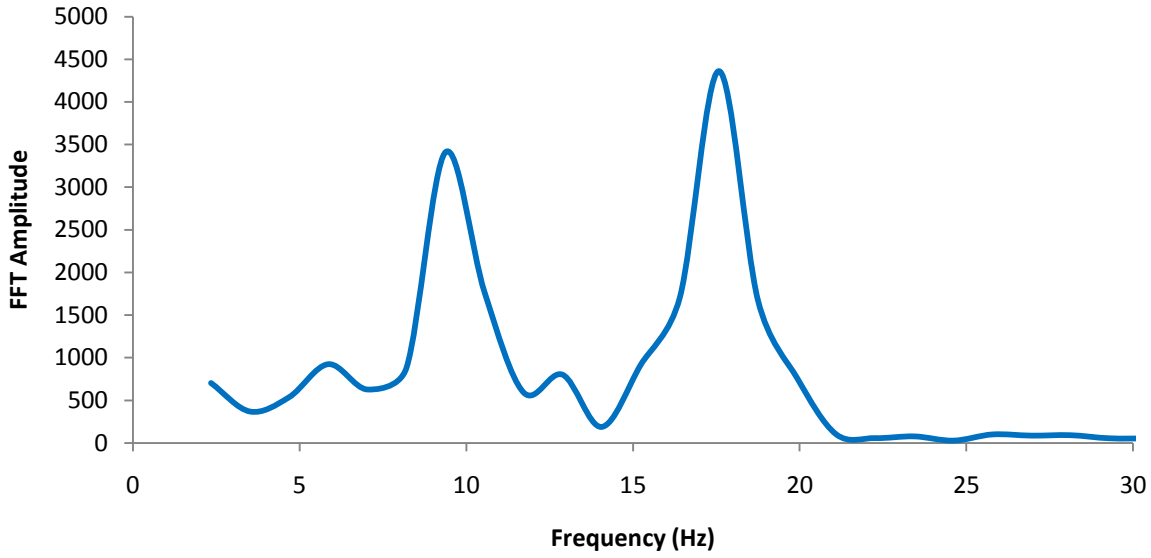

Figure 11: Fourier spectrum for initial mount design [2.5g wire applied wire mass, 5mm wires, total system mass(diamond plus wires) of .25g]

This spectrum gives a fundamental frequency of 17.57 Hz, below the theoretical value. This indicated that either the fiber bundle was losing tension or there was an error in how the tension was being applied. A test was performed in order to validate the loss of tension hypothesis, in which the wires were artificially weighted and the tension determined based on the natural frequency of the fiber bundle.

4.4 Validation of tension loss hypothesis

In order to determine if the wires were losing tension it was important to analyze the wires separate from the diamond. The issue with analyzing just the wires is that the fundamental frequency of the wires, even at relatively low tensions, is very high, well beyond the imaging rate of our camera. If we assume that the carbon fiber bundle is one fiber with an effective linear density of

$$\rho_{effective} = n\rho_{fiber} \tag{11}$$

where n is the number of fibers then the fundamental frequency is:

$$f = \frac{1}{2L}\sqrt{\frac{T}{\rho_{effective}}} \tag{12}$$

In this equation the L is the wire length and T is the applied tension. For this mount, 10 fibers were used, each with a length of 1.5mm and the total applied tension was .0731N. For this fiber bundle the fundamental frequency would be $f \approx 17kHz$. This is well beyond the imaging capacity of the camera used in this experiment which has a video capture rate of 1200Hz. In order to analyze the tension the fiber bundle was artificially loaded with a mass which was significantly more massive than the wires themselves.

In order to achieve this weighing a small glue ball was added to a mounted 10 fiber bundle. The ideal natural frequency of the mass and fiber bundle system was found to be 201Hz. The mount was then vibrated using a stereo speaker at specific frequencies. Since the

wire would have a vibration response when driven at its natural frequency it would be possible to determine the vibration frequency if the right tone was selected. A tone generating program, the NCH Tone Generator was used to generate a single frequency tone. This frequency was then changed small amount at regular intervals until vibration was seen in the fiber. Originally a narrow sweep about the theorized natural frequency was taken. When this yielded no results a sweep over a much larger range was taken. As the vibration response was observed this range was narrowed until the natural frequency was found.

Figure 12: Image of the fiber bundle driven at resonance (left) and at a frequency just beyond resonance (right)

The two images show the effect of driving the wire at resonance and away from resonance. In the image on the left the wire was being driven at its natural frequency. The result is a large vibration response. The image on the right shows the same wire being driven .1Hz away from resonance. There is almost no visible response in the vibration of the wire. The left image was taken at 62.12 Hz, well below the theorized natural frequency. This analysis confirmed that the wires were losing tension. This analysis, coupled with initial Fourier

analysis, indicated that a redesign of the mount and a change in mounting procedure was necessary.

4.5 System redesign

4.5.1 Changing from tungsten to carbon

One important decision which was made during the beginning stages of this project was to change from tungsten fiber to carbon for mounting the diamond. One of the main concerns is the amount of background radiation which the mount will produce. In order to determine the amount of background noise, the bremsstrahlung cross section needed to be determined. The research done by Fano, et al. showed a Z^2 dependence on the bremsstrahlung cross section. All other things being equal, the number of photon producing events for a particular energy k scales at the cross section. Therefore the number of photon events for a carbon fiber is ~90 times less than the number of photon events for a tungsten fiber of the same thickness. Also carbon fibers have a higher ultimate tensile strength (~5600MPa versus 1510 MPa) so the carbon fiber bundle can actually be smaller than a tungsten fiber bundle of the same tensile strength.

4.5.2 Mount redesign

The results of the video analysis for the initial mounting scheme resulted in the need to redesign the mount. The initial design had two brackets, a top and a bottom, which held the wires in place. This necessitated tensioning the wires together because the bottom bracket spanned both wires. The redesigned mount uses a split bottom bracket to allow each fiber to be tensioned individually. Also, each bracket has a second attachment point to the back plate. This ensures that the wire tension is sufficiently held.

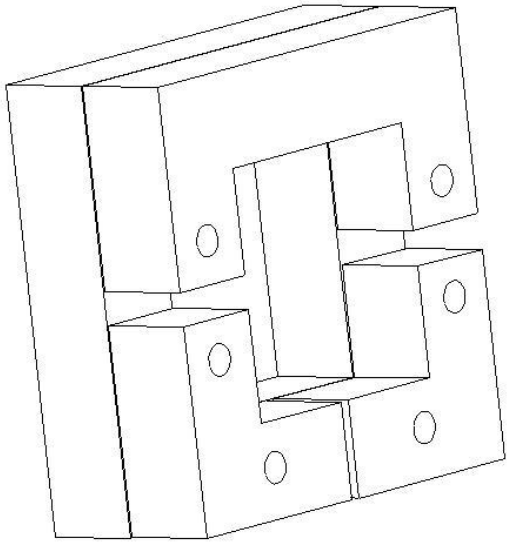

Figure 13: Cad image of redesigned mount

4.5.3 Tensioning apparatus design and construction

Initially the mount design necessitated that both fibers be tensioned simultaneously using the same weight. Below is an image of the initial tensioning rig. The 5g weight is located in the lower right hand side of the image.

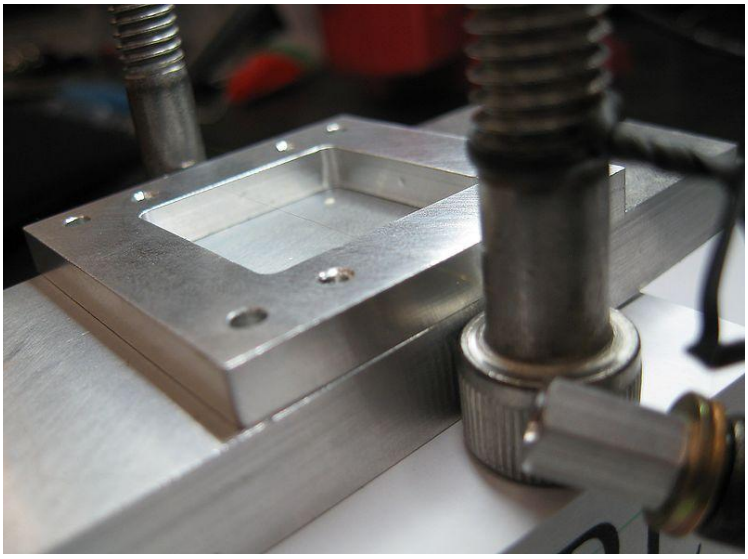

Figure 14: Initial wire tensioning device for tungsten fibers

The simultaneous tensioning proved to not only be difficult but ultimately unreliable. It is difficult to determine whether both fibers are receiving an equal share of the applied weight. This unequal weight distribution would cause the diamond to rotate about each axis unequally making predictions about the vibration frequency unreliable. To rectify this, a tensioning device which tensions an individual fiber was designed and constructed

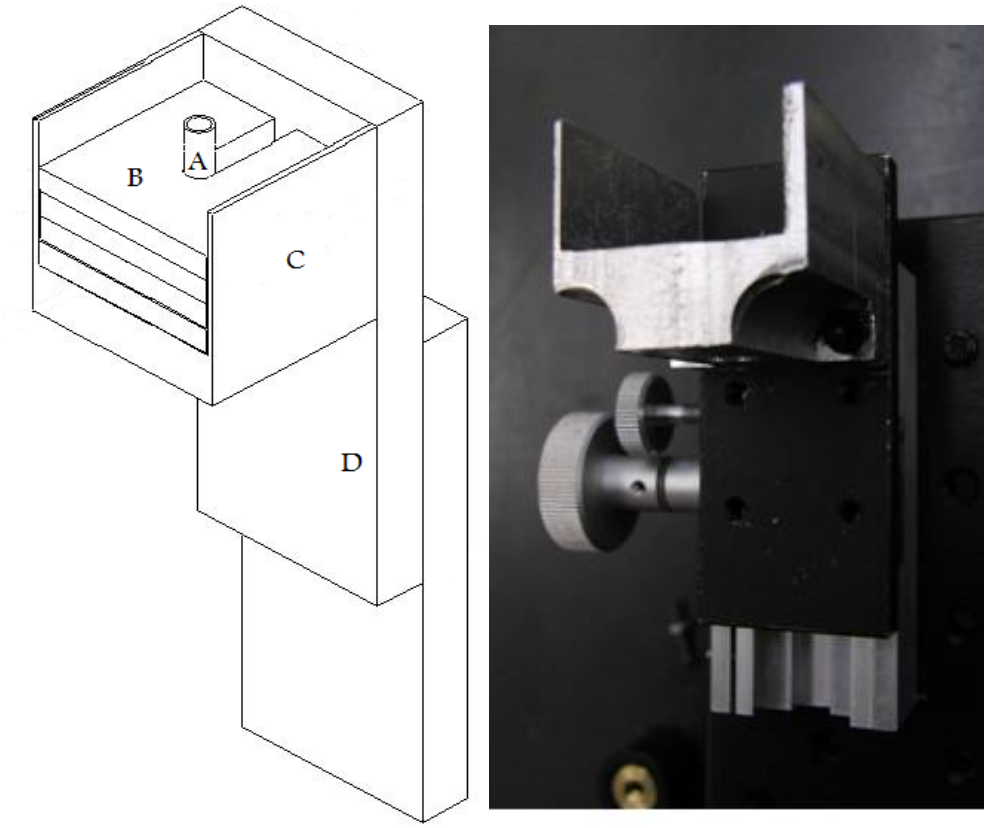

Figure 15: Cad drawing and image of the redesigned tensioning device

The fiber bundle is threaded through the central hub (A) to which several weight plates (B) are attached. These plates are in a carriage (C) which can be raised and lowered using a linear translation stage (D). The fiber bundle is mechanically attached to the central hub. When the carriage is lowered, the weights and hub remain stationary, removing the weights from the carriage. The weight tensioning the fiber bundle is then free floating. This ensures that all of the applied weight is being supported by the bundle, giving very accurate tensioning of the fiber bundles.

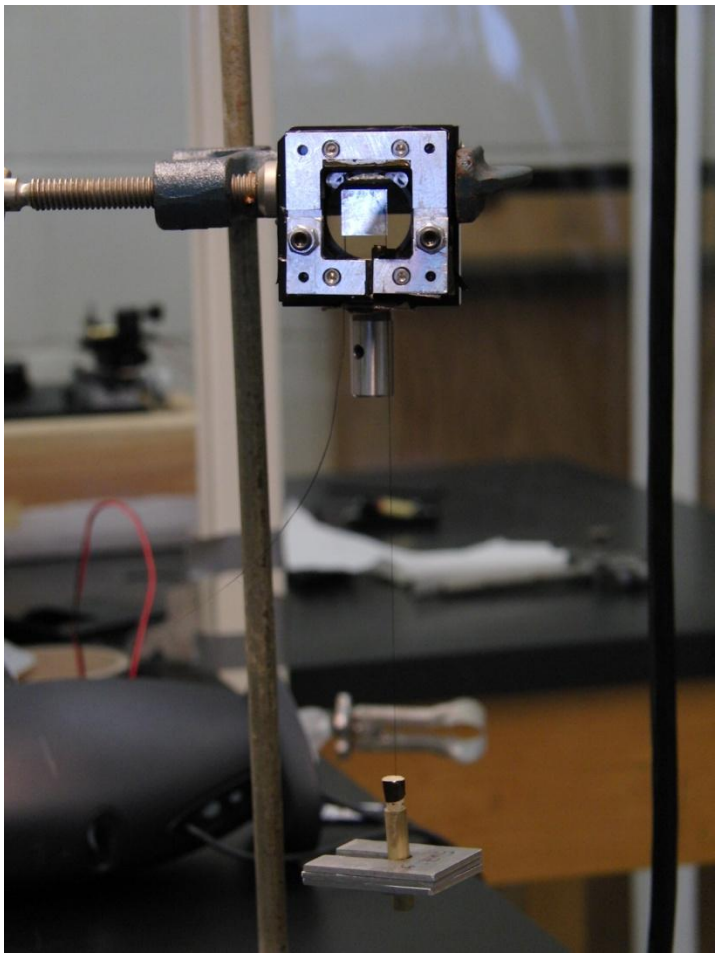

Figure 16: Image of the strung diamond mount showing the tensioning process

Using this newly designed mount and tensioning device the effects of natural frequency versus tension were analyzed and compared to the theoretical values based on the first order approximation.

5. Results of fiber bundle tensioning

Once the mount was redesigned and the tensioning apparatus built analysis of the frequency versus applied mass needed to be done. Six weight plates with a mass of 5.74±.1g were constructed. The tension was varied by varying the number of plates added, from 5.74g to 34.4g. The position versus time was recorded for each successive plate addition and the Fourier spectrum was analyzed. When analyzing the spectrum it became apparent that the vibration about the x axis was not a concern. Even for these low tensions the vibration amplitude was at or near our divergence specification and the belief is that this mode of vibration will not be a factor in the final design. Because of this only the vibration about the y axis data is presented. (The position versus time and Fourier spectrum analysis for the vibration about the x axis can be found in appendix A.4)

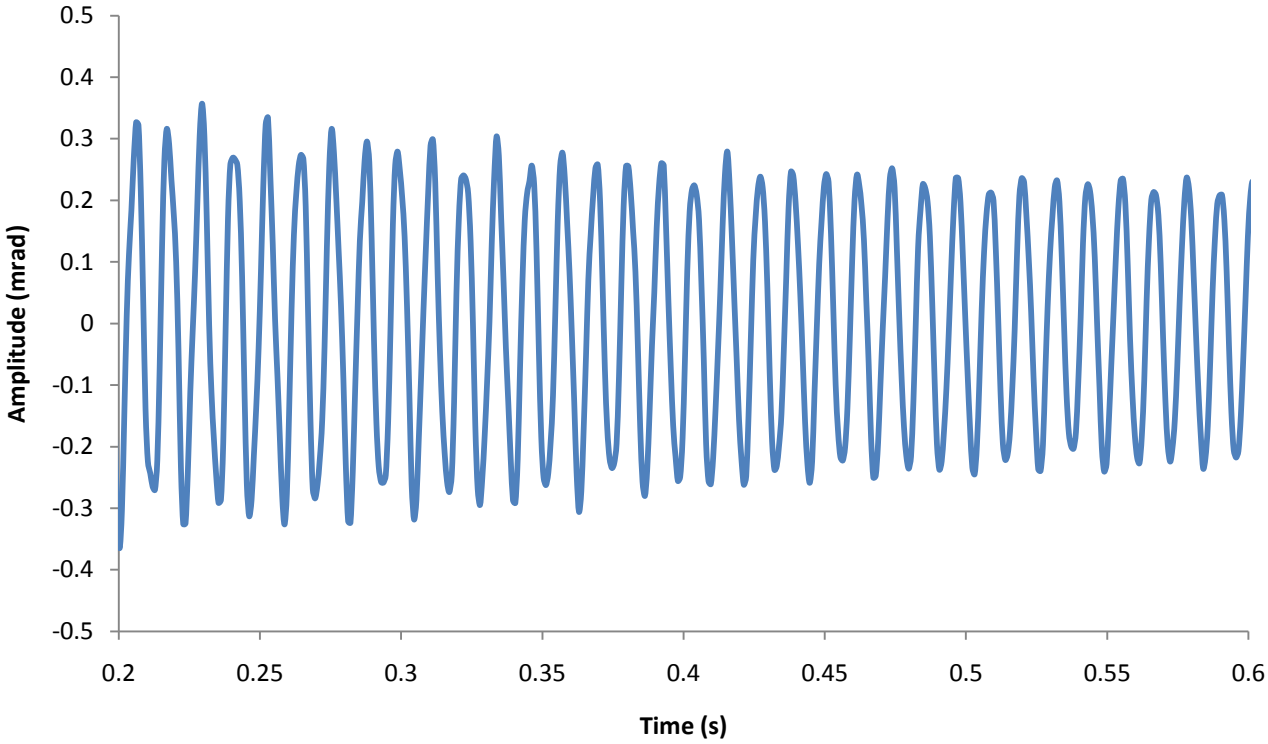

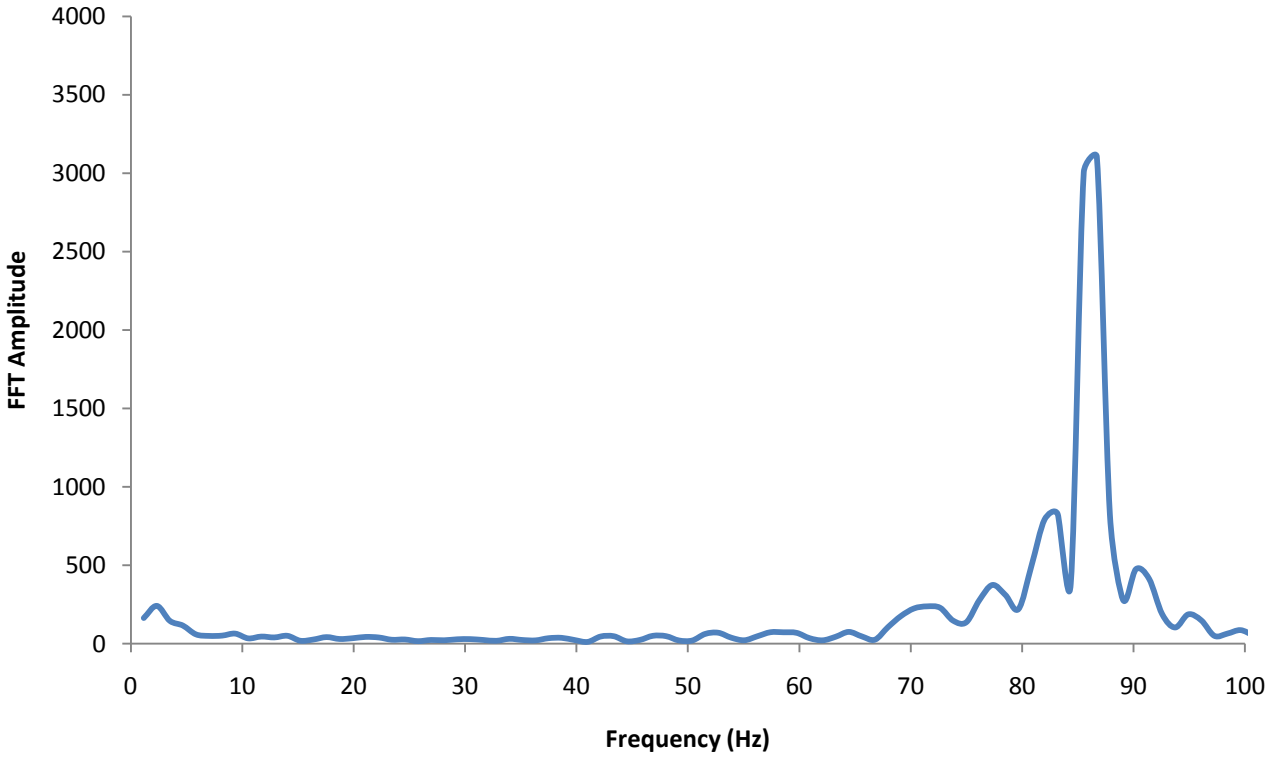

Figure 17: Angular divergence versus time and Fourier spectrum for 34.7g applied mass

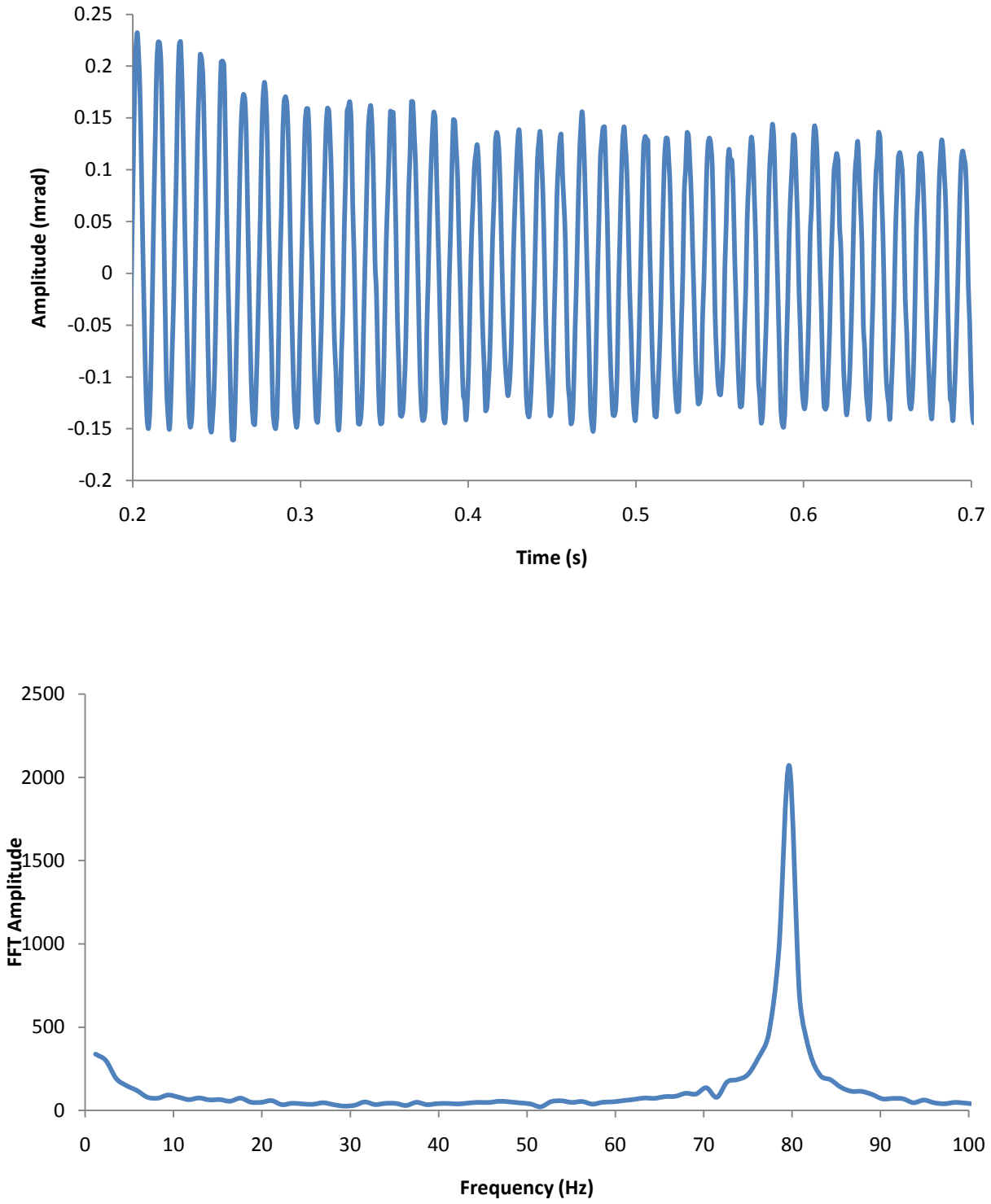

Figure 18: Angular divergence versus time and Fourier spectrum for 28.9g applied mass

As expected the frequency for this applied mass is lower than the first set. For this data set there is an interesting low frequency component. Looking at the rotation about the x axis versus time and analyzing its spectrum gives a clearer picture of the source of the low frequency component.

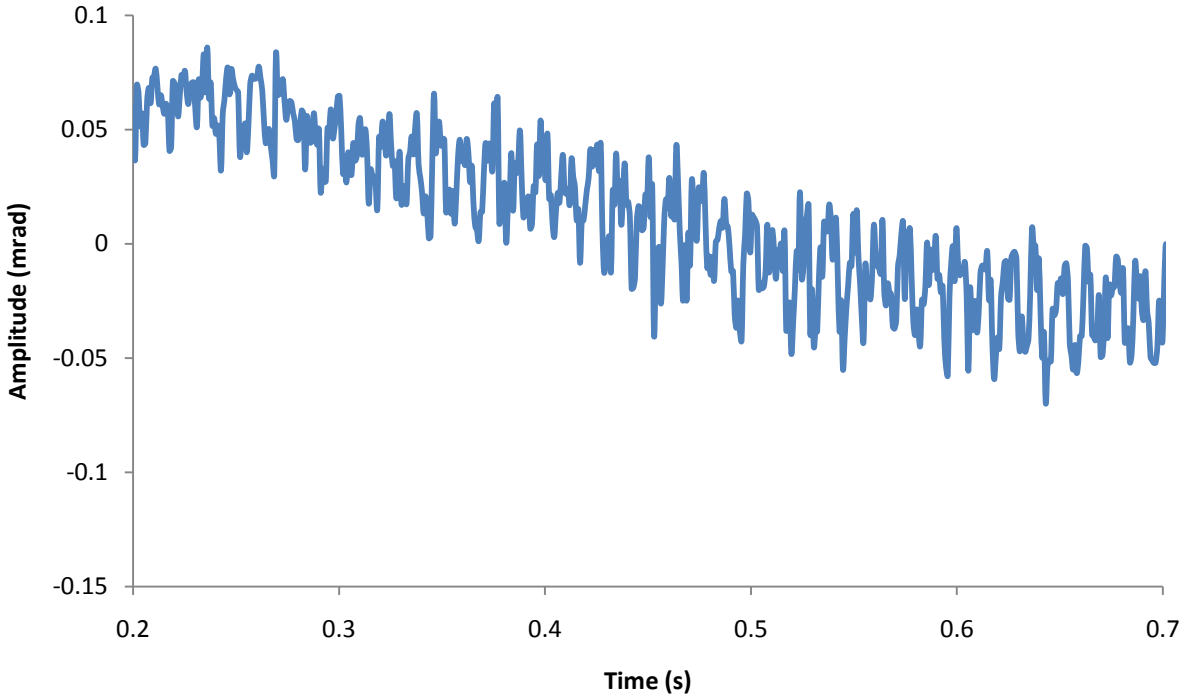

Figure 19: Rotation about the x axis versus time, 28.9g applied mass

Looking at this data it is clear that the camera had moved slowly downward during the talking of this data set. Analysis of the Fourier spectrum further emphasizes this point.

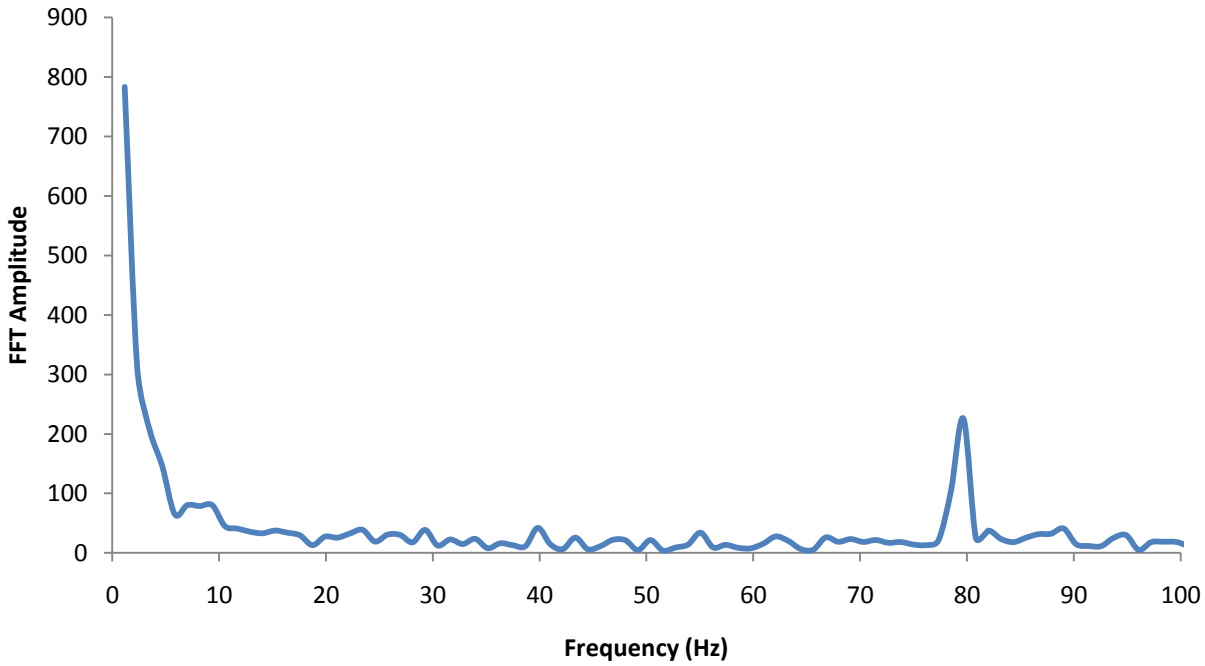

Figure 20: Fourier spectrum for rotation about the x axis, 28.9g applied mass

There is a very strong frequency component around 2Hz. This makes sense since the data for this spectrum was taken over a .5s interval, and the vertical position of the camera was moving the entire time.

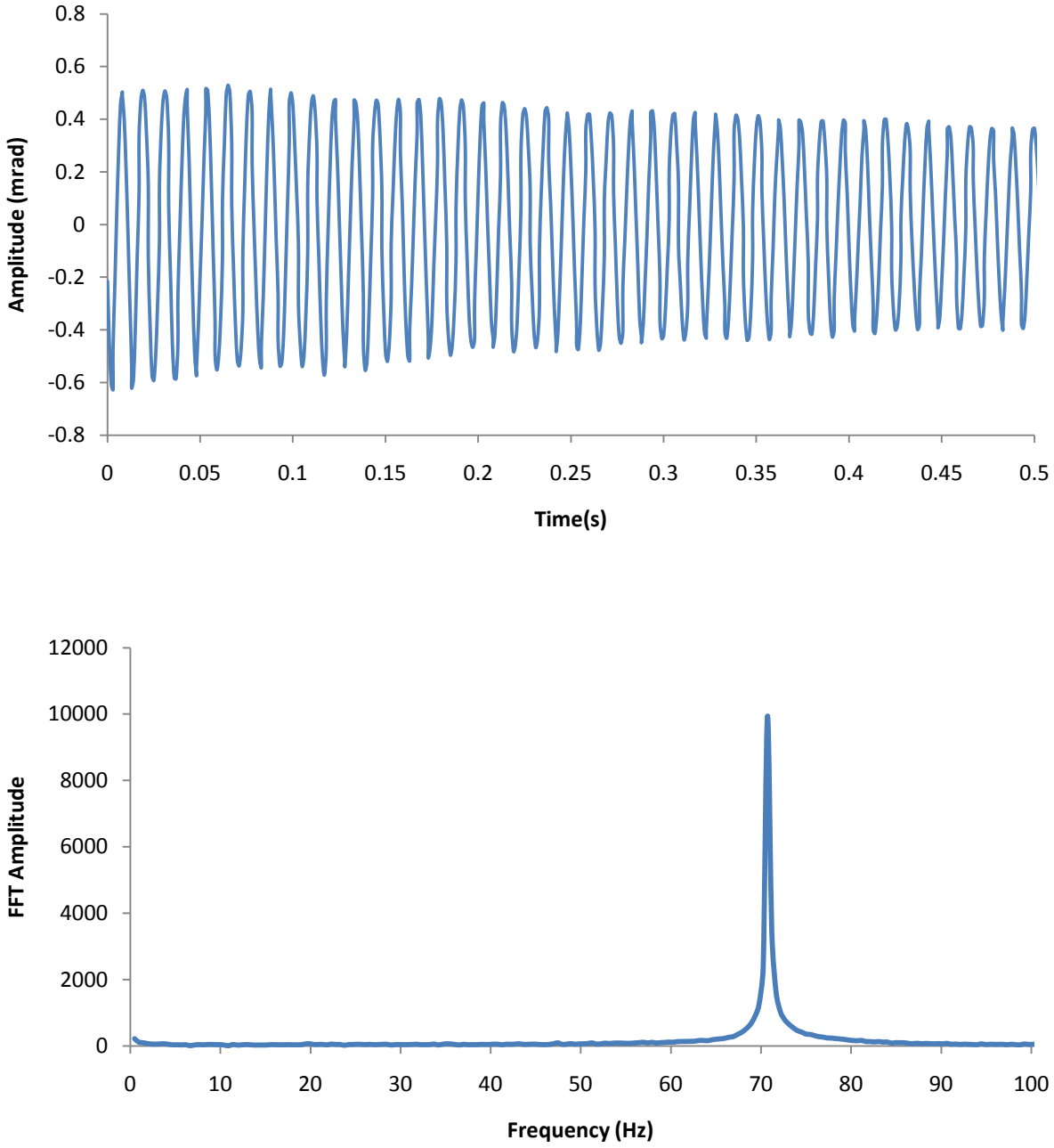

Figure 21: Angular divergence versus time and Fourier spectrum for 23.12g applied mass

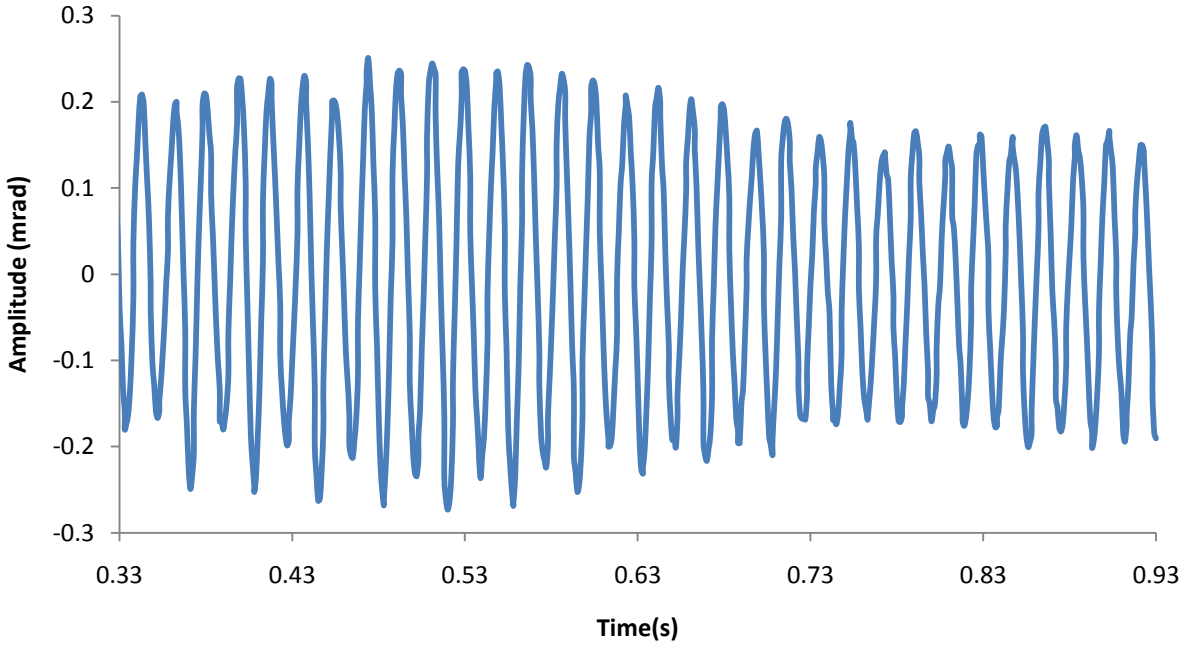

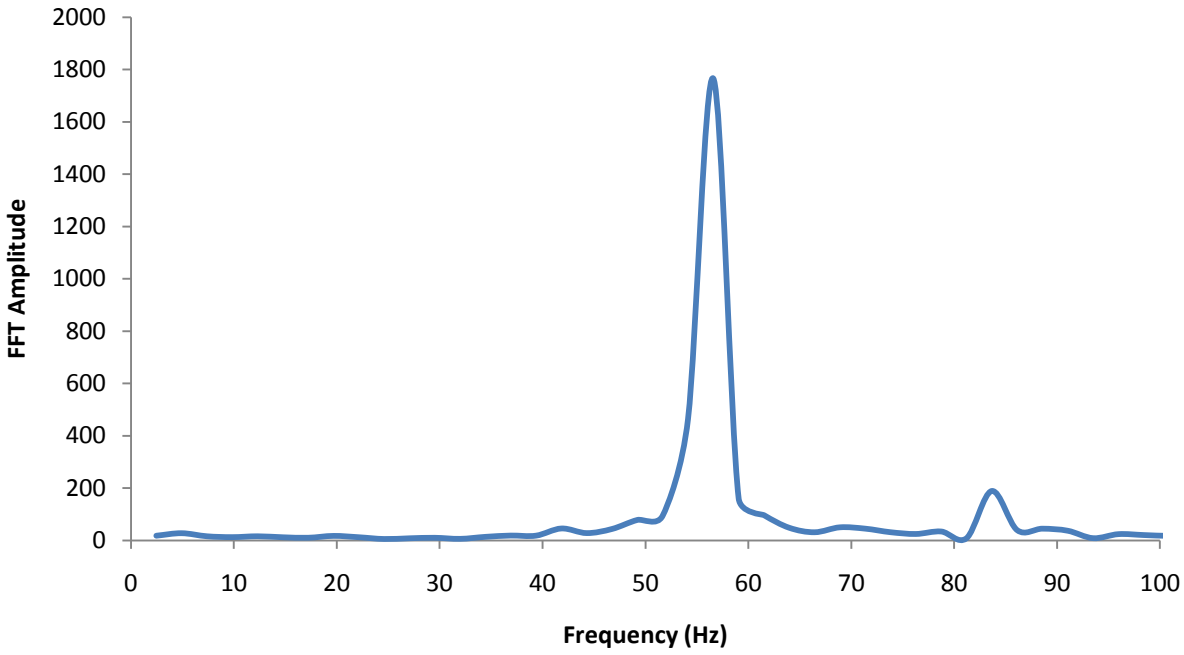

Figure 22: Angular divergence versus time and Fourier spectrum for 17.4g applied mass

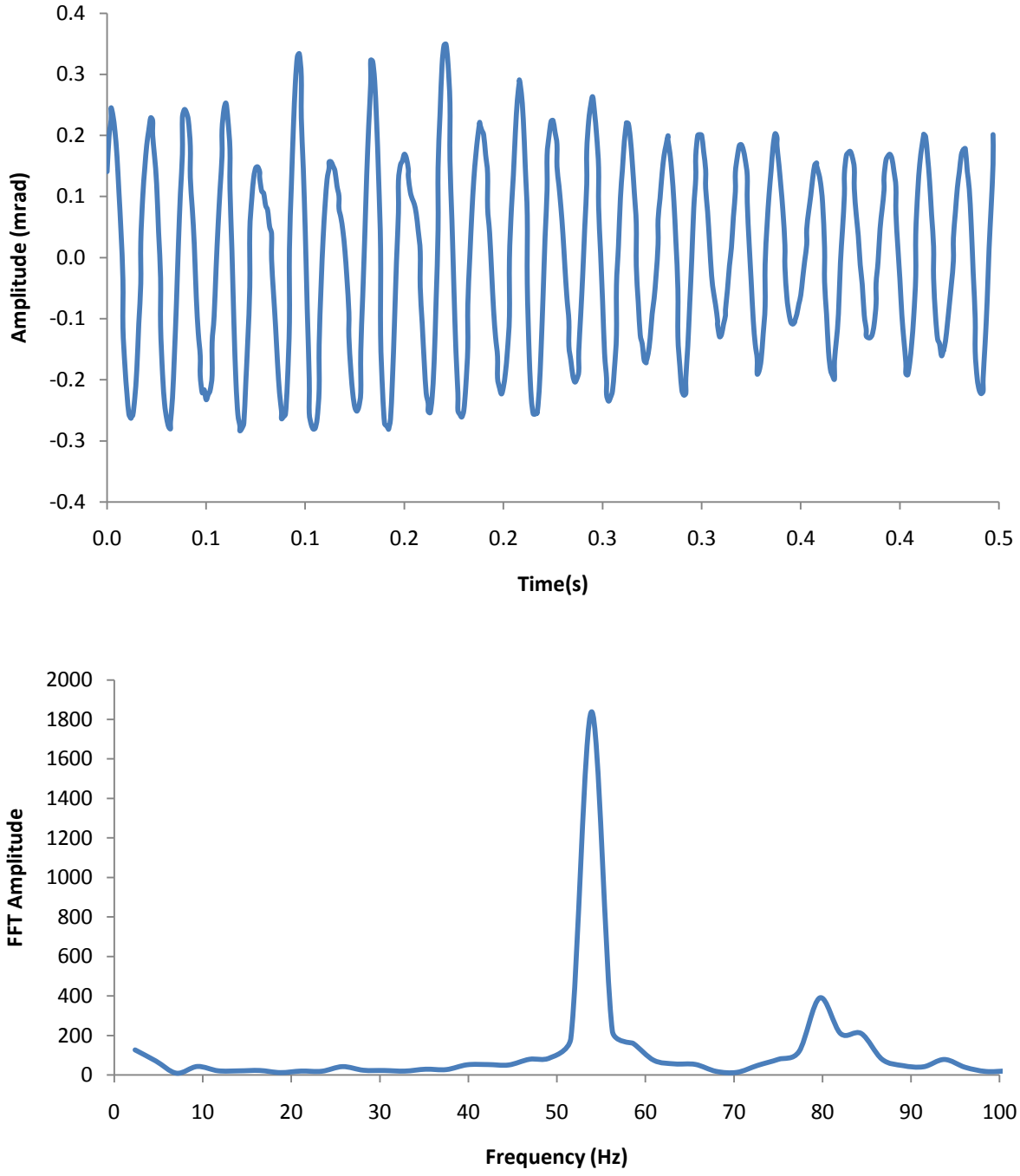

Figure 23: Angular divergence versus time and Fourier spectrum for 11.56g applied mass

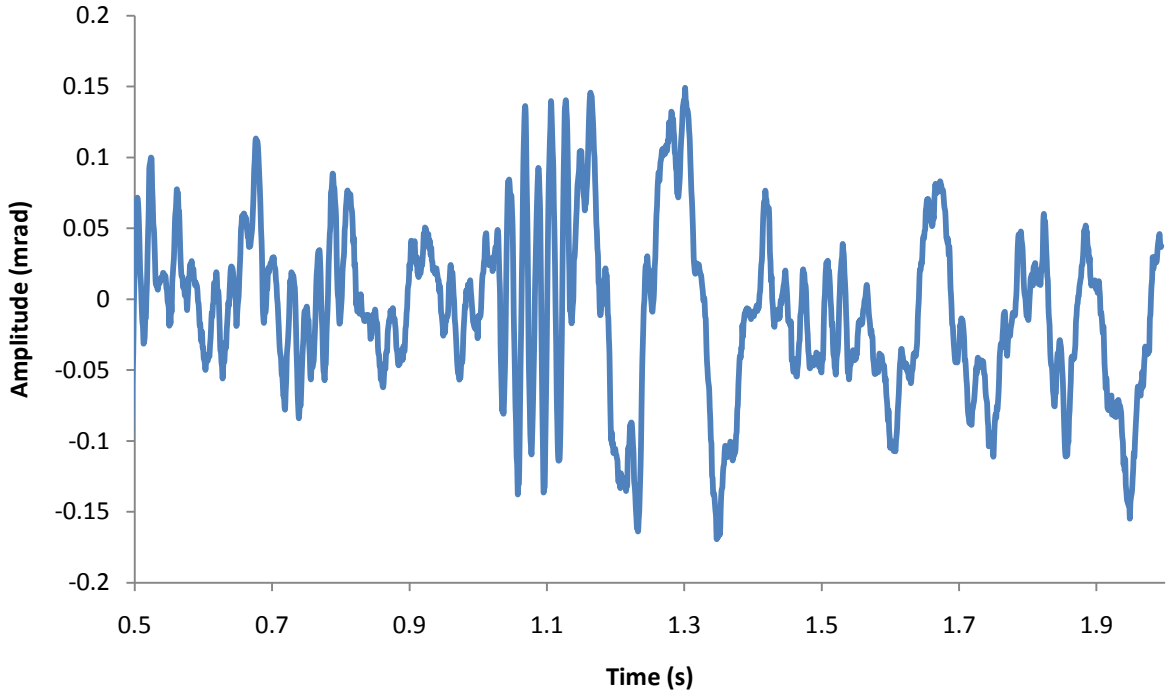

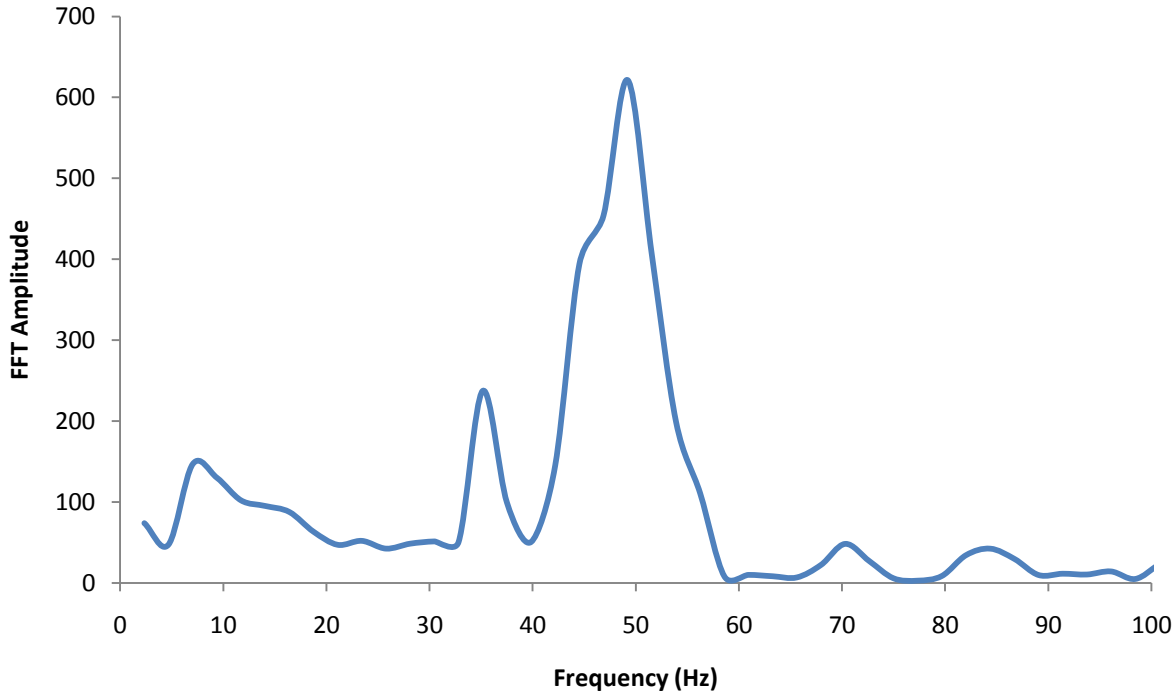

Figure 24: Angular divergence versus time and Fourier spectrum for 5.78g applied mass

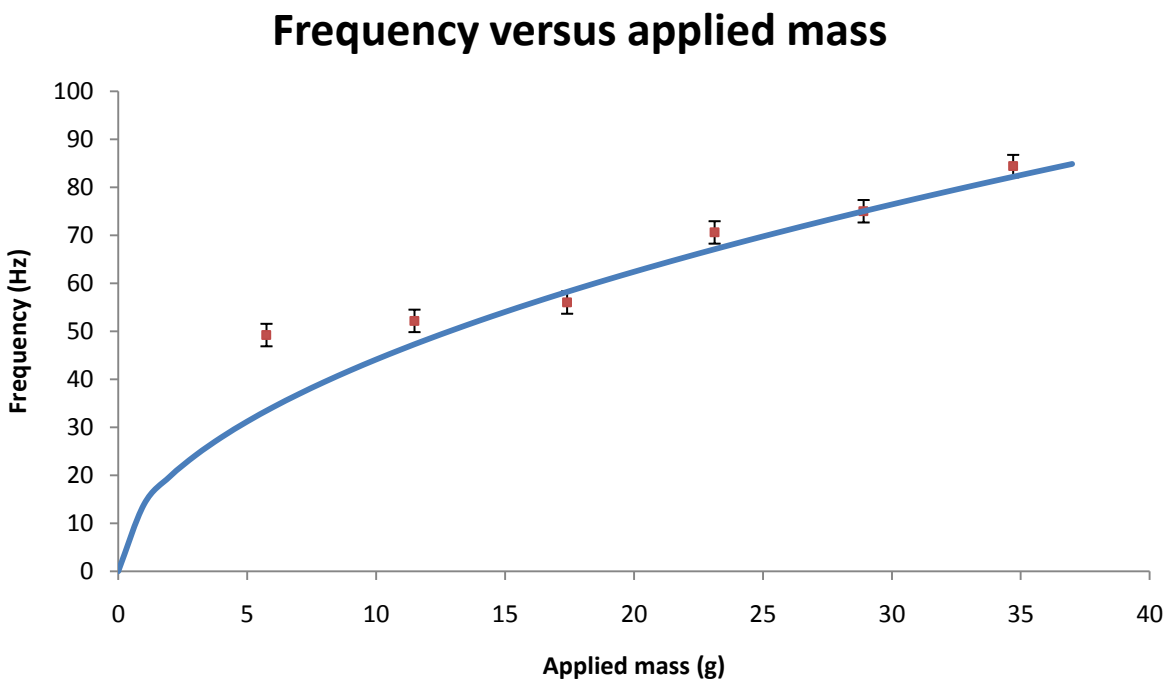

Figure 25: Frequency versus applied mass for the first order approximation and the recorded data

Again, the first order approximation for the frequency versus tension is

$$f = \frac{1}{\pi}\sqrt{\frac{F_T}{Wm}} \qquad (13)$$

shown in blue. The data points obtained from the Fourier analysis for the various positions versus time graphs are shown in red. The data points fit the graph well for higher tensions so it is valid to use the first order approximation to determine the tension needed to make the natural frequency over 500Hz. By extrapolating the theoretical curve it can be shown that the required applied mass to reach 500Hz is 1275g. Each fiber can safely hold 7g. This means that with the current mount it would take 183 fibers to hold the required applied mass.

6. Conclusions

The work for this project focused on imaging and quantifying the vibration of a diamond radiator in a suspended mount. The motivation behind this work was the analysis done on the rocking curve spectra for a diamond radiator performed at CHESS. This rocking curve indicated that stability in diamond mounting was a significant factor in how the radiator performed. A direct imaging technique was developed for analysis of the diamond vibration. This involved the use of a coherent 532nm laser to view the rocking of the diamond plane.

Testing on the initial mount design was done, indicating there were several issues with the initial design. Among these were issues with loss of tension of the fibers as well as issues with insuring each wire was properly tensioned. These issues were rectified by redesigning the mount, as well as developing a new technique for fiber tensioning. One the redesign was complete a series of tests were performed to analyze the system response at low vibration frequency. The data obtained from these tests was compared to a first order approximation of the vibration frequency and was found to match for frequencies in the 60Hz+ range, but diverged slightly from the test results for lower frequencies. Since the first order approximation is valid for higher tensions it can be used to estimate the tension necessary to reach the desired 500Hz frequency. For the current mount this value is shown to be 1275g. Other techniques, including reducing the fiber length will need to be investigated in order to reduce the necessary amount of applied mass.

7. Future Work

There are several steps that can be taken in the future to continue this research. Now that the system response is well understood for low frequency vibration, the interferometer can be used to analyze higher frequency vibration. Ideally, the mount would have a natural frequency in the 500Hz+ range. This is near the maximum operating range of the imaging device. Again, for this camera the maximum frequency which can be recorded is 600Hz. Similar to the low frequency analysis, it may be useful to measure frequency versus tension below 600Hz and interpolate the data to find the tension necessary to give the desired frequency.

Also the impact of the number of carbon fibers needs to be explored. It is desirable to have a small number of carbon fibers while still being able to adequately hold tension for two reasons. First, the generation rate of background photons is directly related to the thickness. While the change from tungsten to carbon has significantly lowered this background noise, this background can be further reduced by reducing the fiber bundle size. Second the proportion of usable diamond surface (the fraction of diamond at least one σ_h away from the fiber) increases as the fiber size decreases. This will increase the amount of time which each diamond can be used for and will reduce the number of diamonds needed over the lifetime of the project.

Besides the continued vibration analysis which needs to occur there are other areas which the use of the interferometer will be useful for. One such area is the analysis of the ablated diamonds, both through in-house Interferometry and rocking curve analysis at CHESS. For the former, a new technique for mounting the diamonds on the carbon fiber bundle needs to be developed. Currently glue is used to hold the simulated diamond on the fibers, but it is

believed that this technique will be too damaging to thin diamonds. Techniques are currently being investigated including a modified sintering technique in this the carbon fiber is mechanically fused to the diamond.

For the later a more stable ring mount has been developed. This mount consists of two stretched Mylar sheets between which the diamond rests. The hope is that the Mylar can be stretched sufficiently to create a center section which is optically flat to below our divergence specifications. In order to analyze the flatness of the Mylar sheets, they will be images using the interferometer. The mount will be rastered using a 3-d translation stage which will allow for most of the surface to be analyzed. The interference pattern will be recorded and the change in pattern analyzed as the mount moved relative to the laser spot.

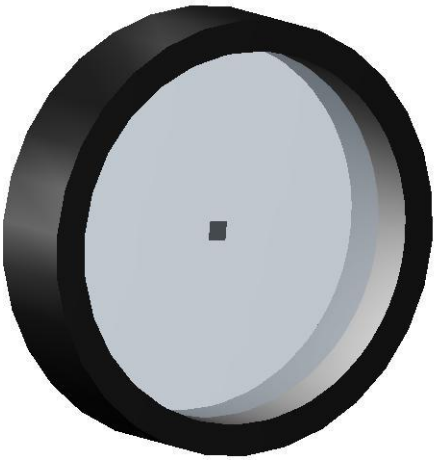

Figure 26: Ring mount for diamond analysis at CHESS

Acknowledgements

There are several people I would like to thank for their help and support during this project. First I would like to thank Dr. Richard Jones for the opportunity to work on this project. Without your help and guidance this project would not have been successful. Second I would like to thank Igor Senderovich. Without your patience and expertise in all things Matlab I may still be trying to code that tracking program a year later. Thanks goes out to Jim McIntyre and Brendan Pratt who were always ready with a helpful hand or a funny Youtube video.

I would like to thank my parents for their support for the last 23 years. Without you none of this work would be possible. Special thanks go out to Liz Didan. Without your love and support over the past four years I would not be the person I am today.

Appendix A

A.1 Parts list for Michelson Interferometer

Category	Item	Description
Beam Splitter	Beam Splitter Cube	$(2cm)^3$,AR,400-700nm
	Kinematic Platform Mount	$(2in)^2$
	Prism Clamp	Large Clamping arm
Camera	Casio Ex-F1	
Mirrors	Protected Silver Mirror	25.4mm Dia., R≈98%
	Mirror Holder	Standard 1" holder
	Kinematic mirror Mount	Adjustable Kinematic Mount for 1" holder
Light Source	532nm Green laser Module	5mW, 5mm spot size, <1.4 mrad div.
	Kinematic V-Mount	Small mount with attached Clamping Arm
Beam Expander/Spatial Filter	Pinhole	5μm, 10 μm, 15 μm and 20μm pinholes
	Pinhole Mount	½" and 1" standard holder
	Small Plano-Convex Lens	f=50mm, 12.7mm Dia., AR coating
	Large Plano-Convex Lens	f=200mm, 25.4mm Dia., AR Coating
	Lens Holders	Holders for ½" and 1" optics lenses
Translation Stages	Small Linear Translation Stage	
	3-Axis Translation Stage	
Common Mechanics	Posts	¾" and 1" high posts, ½" Dia.
	Post Holders	

A.2 Determining proper converging lens dimension and focal length

In order to determine the proper converging lens diameter and focal length the pattern which the beam makes as it passes through the pinhole needs to be analyzed. The object of this analysis is to give a general equation for the area of the first maxima and then to apply that to a special case which matches our experimental set-up. Through analysis of Maxwell's equation, it can be found that the amplitude as a function of position from the beam line as

$$A(r') = -\frac{1}{2\pi}\int_{z=0} d^2r \left(\frac{A(r, t' - \frac{|r-r'|}{c}}{|r-r'|^3}(-z') + \frac{1}{c}\frac{\dot{A}(r, t - \frac{|r-r'|}{c}}{|r-r'|^2}(-z') \right) \tag{14}$$

$$A(r') = -\frac{1}{2\pi}\int_{z=0} d^2r \left(\frac{A(r, t' - \frac{|r-r'|}{c}}{|r-r'|^3}(-z') + \frac{1}{c}\frac{\dot{A}(r, t - \frac{|r-r'|}{c}}{|r-r'|^2}(-z') \right) \tag{15}$$

In our case we consider only terms that drop off as r'. So

$$A(r') = \frac{z'}{2\pi c}\int_{z=0} d^2r\left(\frac{A(r, t - \frac{|r-r'|}{c}}{|r-r'|^2}\right) \tag{16}$$

$$A(r') = \frac{ikz'}{2\pi}\, e^{i\omega t'}\int_{z=0} rdrd\phi\frac{e^{ik|r-r'|}}{|r-r'|^2}A_0(r,0) \tag{17}$$

In this case we will consider light passing through a circular disk of radius a. This will ultimately be a function of the Bessel Function of the first kind for order 1.

Let

$$\mathcal{I}(r) = \int_0^a rdr\int_0^{2\pi} d\phi\frac{e^{ik|r-r'|}}{|r-r'|^2} \tag{18}$$

Then

$$A(r') = \frac{z'A_0}{2\pi c}e^{ikct'}\mathcal{I}(r') \tag{19}$$

But

$$|r-r'| = \sqrt{(x-x')^2 + (y-y')^2 + z^2} \tag{20}$$

$$= \sqrt{r^2 + r'^2 + 2r\rho^2 cos\phi} \tag{21}$$

$$= r' - \frac{2r\rho' cos\phi}{2r'}, \frac{\rho'}{r'} = sin\theta' \tag{22}$$

So that

$$|r - r'| = r' - rcos\phi sin\theta' \tag{23}$$

and

$$\frac{1}{|r - r'|^2} \approx \frac{1}{r'^2}\left(1 + \frac{2rsin\theta' cos\phi}{r'}\right) \tag{24}$$

In this particular case, we are dealing with far-field effects only, so

$$\frac{2rsin\theta' cos\phi}{r'} \to 0 \; and \; \frac{1}{|r - r'|^2} \approx \frac{1}{r'^2} \tag{25}$$

So,

$$\mathcal{I}(r') = \int_0^a rdr \int_0^{2\pi} d\phi \frac{e^{ik|r-r'|}}{|r - r'|^2} \tag{26}$$

$$= \frac{e^{ikr'}}{r'^2} \int_0^a rdr \int_0^{2\pi} d\phi e^{iksin\theta' \cos\phi} \tag{27}$$

The integral $\int_0^{2\pi} d\phi e^{iksin\theta' \cos\phi}$ is the integral representation of the zero order Bessel function of the first kind with $krsin\theta'$ as the argument. This gives us the equation:

$$\mathcal{I}(r') = \frac{e^{ikr'}}{r'^2} \int_0^a rdr 2\pi J_0(krsin\theta') \tag{28}$$

To simplify the math, we make use of the fact that we can represent this Bessel functions as the derivative of a Bessel function of a different order. In general, the formula to compute this derivative is

$$z^{v-k}J_{v-k}(z) = \left(\frac{1}{z}\frac{\partial}{\partial z}\right)^{k} z^{v}J_{v}(z) \tag{29}$$

In this case take

$$v = k = 1 \ \ and \ z = krsin\theta' \tag{30}$$

So

$$J_0(krsin\theta') = \left(\frac{1}{krsin\theta'}\frac{d}{d(krsin\theta')}\right)(krsin\theta')J_1(krsin\theta') \tag{31}$$

This gives the equation:

$$\mathcal{I}(r') = 2\pi\frac{e^{ikr'}}{r'^2}\int_0^a rdr\left(\frac{1}{krsin\theta'}\frac{d}{d(krsin\theta')}\right)(krsin\theta')J_1(krsin\theta') \tag{32}$$

Let $x = krsin\,\theta'$ so that:

$$\mathcal{I}(r') = 2\pi\frac{e^{ikr'}}{r'^2}\int_0^a rdr\left(\frac{1}{krsin\theta'}\frac{d}{d(krsin\theta')}\right)(krsin\theta')J_1(krsin\theta') \tag{33}$$

$$\mathcal{J}(r') = 2\pi \frac{e^{ikr'}}{k^2 \sin^2\theta' r'^2} \int_0^{kasin\theta'} dx \frac{d}{dx}\, xJ_1(x) \tag{34}$$

$$\mathcal{J}(r') = 2\pi \frac{e^{ikr'}}{k^2 \sin^2\theta' r'^2} [aJ_1(kasin\theta')] \tag{35}$$

And

$$A(r') = \frac{z' A_{0a}}{c} \frac{e^{ikr'-i\omega t;}}{ksin\,\theta' r'^2} J_1(kasin\theta') \tag{36}$$

To find the angle to the diffraction minimum, we must find the zeroes of this amplitude function. This will occur when $J_1(kasin\theta') = 0$

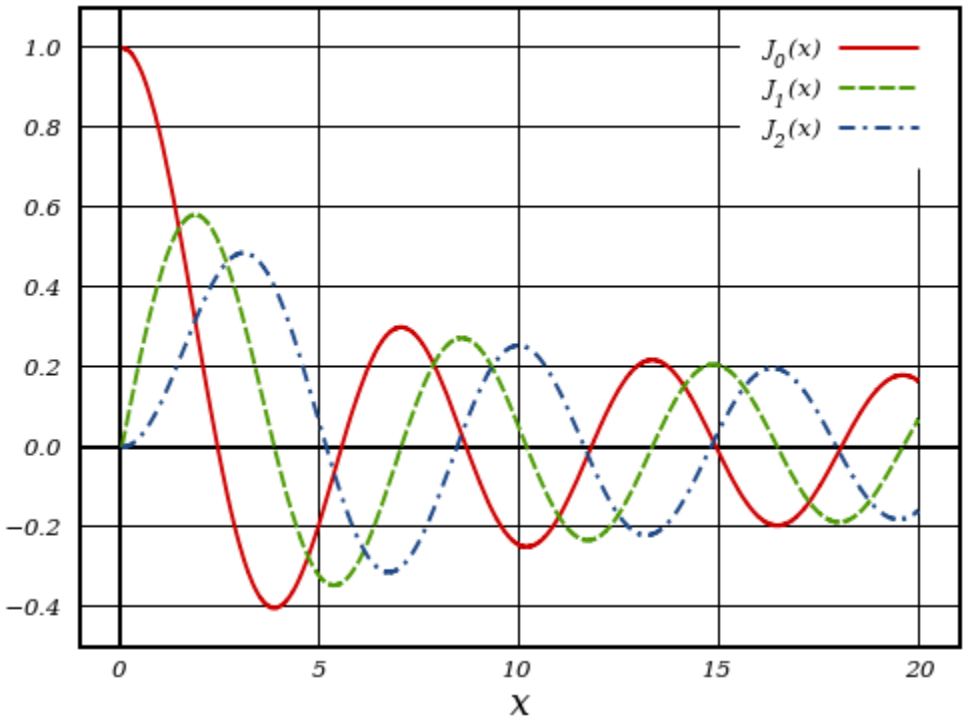

Figure 27: Graph of the Bessel function of the first kind, orders α=0,1,2

Above is a graph of three Bessel functions of the first order, specifically $J_0(X), J_1(x), and\ J_2(x)$. As it is shown, the first zero of $J_1(x)$ will occur at x=0. This will correspond to the center of the pattern, at $\theta = 0$. Here, we would expect a bright spot, so A(r') should be positive and finite. At $\theta = 0$ the term

$$\frac{J_1(kasin\theta')}{\sin\theta'} \tag{37}$$

is positive and finite, so this expression gives the correct amplitude at $\theta = 0$. The next zero of $J_1(x)$ corresponds to the first minimum of the diffraction pattern. In this case, this zero occurs at x=3.832, so

$$kasin\,\theta' = 3.832 \tag{38}$$

Since

$$k = \frac{2\pi}{\lambda} \tag{39}$$

and

$$a = \frac{D}{2} \tag{40}$$

$$\frac{2\pi \sin\theta'}{2\lambda} = 3.832 \rightarrow sin\theta' = \frac{1.22\lambda}{D} \tag{41}$$

This relationship allows for the converging lens to be selected based on the wavelength of the laser light and the diameter of the pinhole. For example, with the 5μm pinhole which was selected and the 532nm light source, the correct lens so that only the first maxima passes through would have a focal length to radius dimension of

$$\frac{d}{f} = \frac{1.22\lambda}{D} = \frac{1.22 * 532 * 10^{-9}m}{5 * 10^{-6}m} = .1298 \quad (42)$$

where d is the diameter of the lens. The standard size lenses are 25.4mm dia. and 12.7mm dia.. In this case the larger lens was selected so that the parallel beam would illuminate the entire beam splitter cube.

$$f = \frac{25.4mm}{.1298} = 195.67mm \quad (43)$$

From this calculation we can see that a f=200mm is sufficient for our applications.

A.3 Matlab code for finding the lens flare location for many frames

```
function batch2(x0,y0,fnamefref,initial,ind)

n=1:336;
m=1:96;

colormap gray;


pars=zeros(ind,2);
badvec=ones(ind,2);

mask=ones(96,336);
mask(62:73,33:60)=0;


x=x0;
y=y0;

for i=initial:ind
    fprintf(1,'processing: %d\n',i)

  fname=sprintf('/scratch/grendlscratch/Video 1-28/%s-%d.bmp',fnamefref,i);

  video=imread(fname);

  a=double(video(:,:,2));

  pars(i,:)=fminsearch(@(par) sum(sum((a(m,n)-gauss2(n,m,par)).^2.*mask)),[x y]);

  if (pars(i,1)-pars(i-1,1))>=5 || (pars(i-1,1)-pars(i,1))>=5 || pars(i,1)>=130 || pars(i,1)<=0 || pars(i,1)-pars(i-1,1)==0
      badvec(i,1)=0;
  end
  if (pars(i,2)-pars(i-1,2))>=5|| (pars(i-1,2)-pars(i,2))>=-5  || pars(i,2)>=96 || pars(i,2)<=0 || pars(i,2)-pars(i-1,2)==0
      badvec(i,2)=0;
  end

  if badvec(i,1)==0
      badvec(i,2)=0;
  end
```

A.4 Complete collection of angular divergence versus time and Fourier spectrum for rotation about the x axis for redesigned mount

Each of these graphs was obtained using the modified mount design. The applied mass quoted is the mass applied to each fiber bundle.

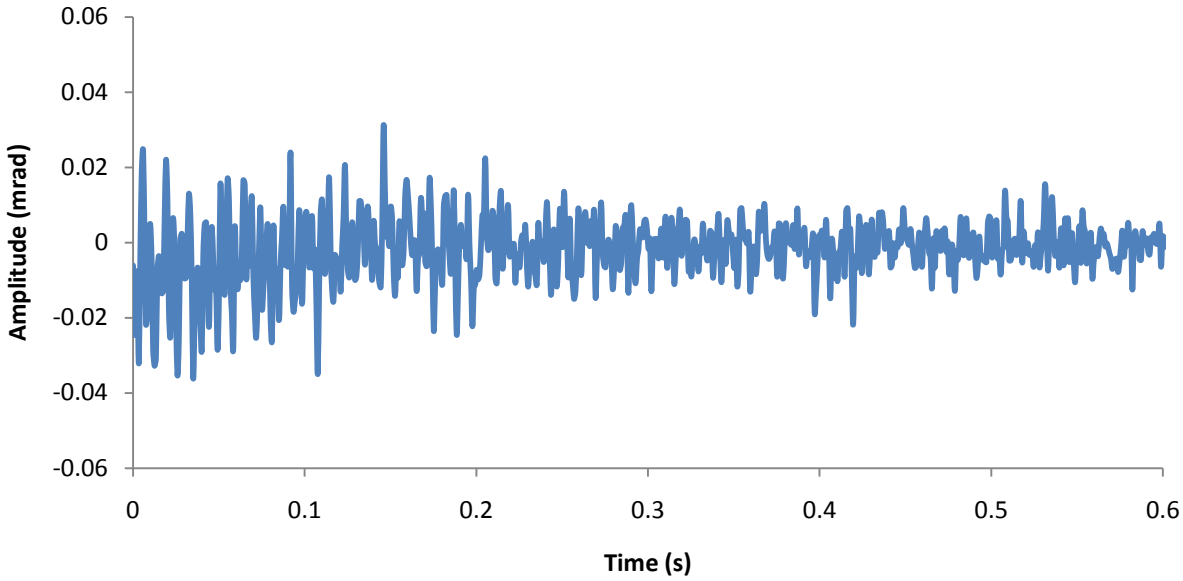

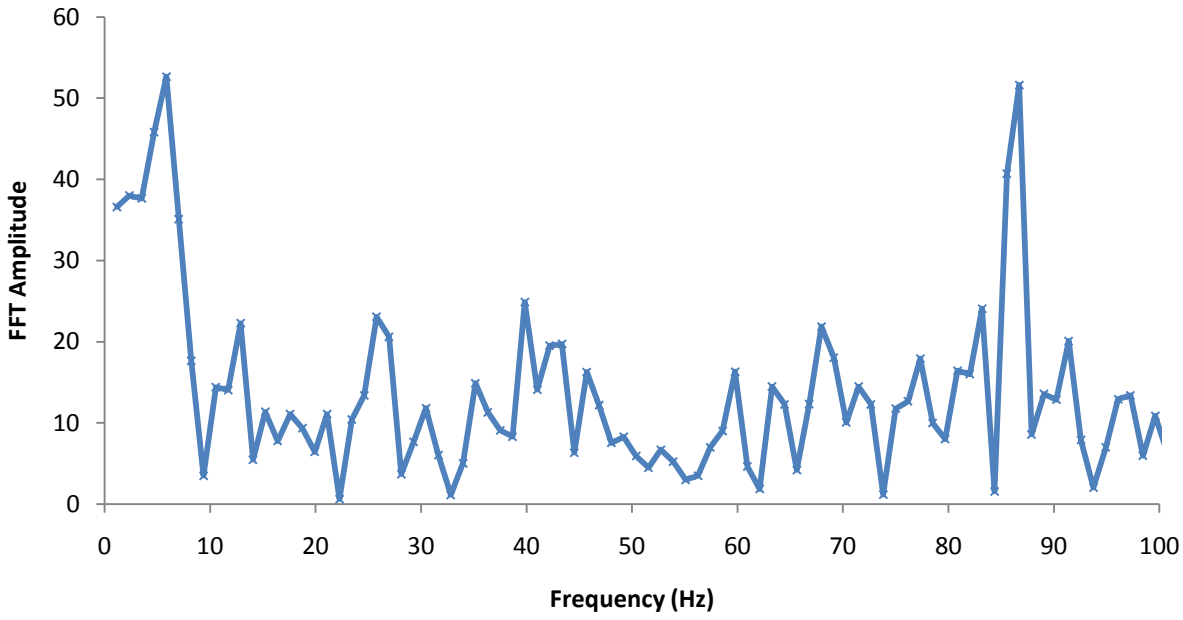

Figure 28: Angular divergence versus time and Fourier spectrum for 34.7g applied mass

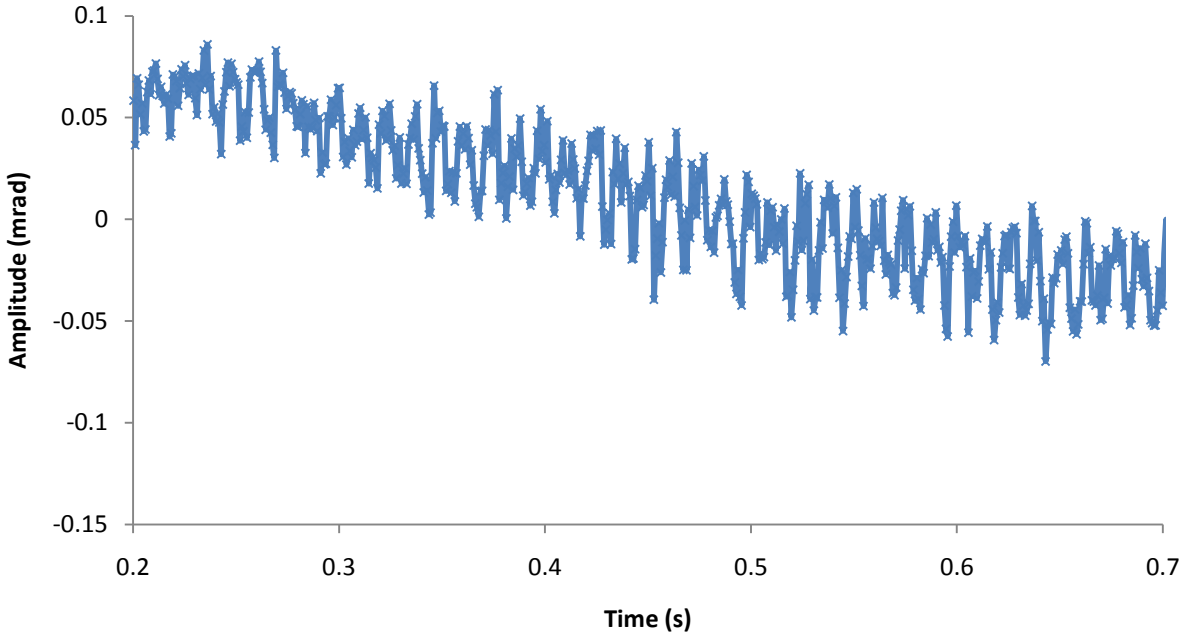

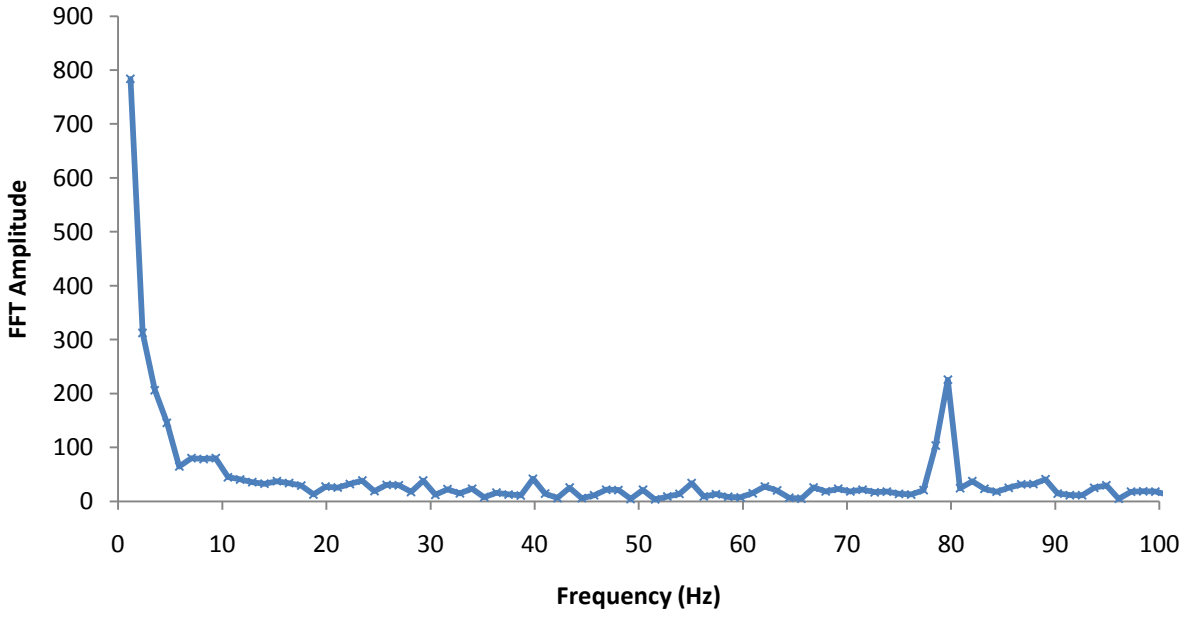

Figure 29: Angular divergence versus time and Fourier spectrum for 28.9g applied mass

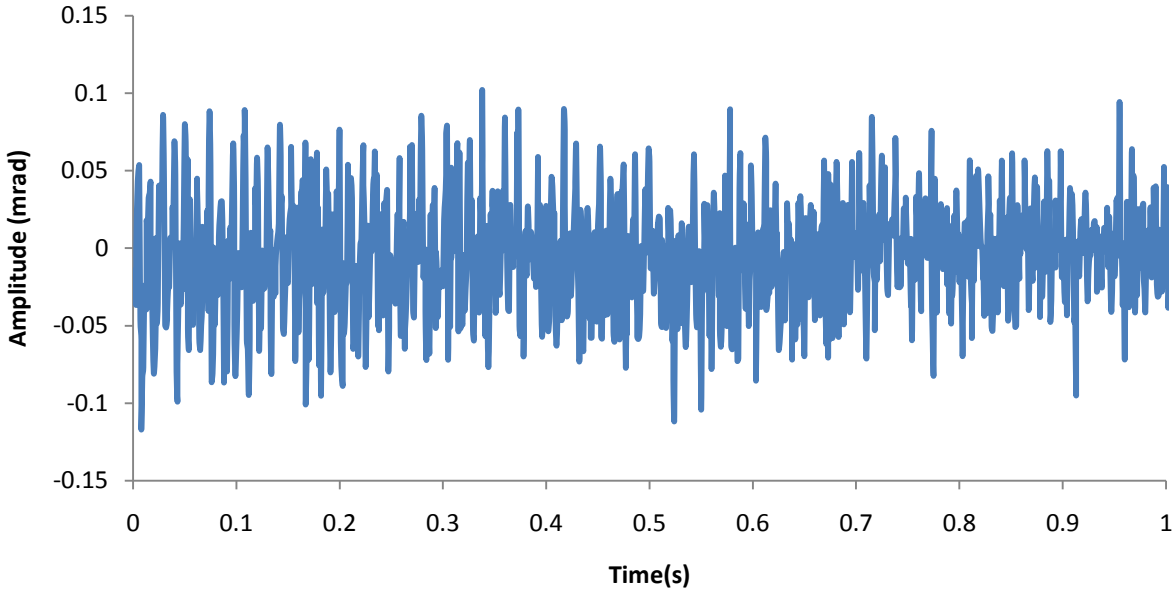

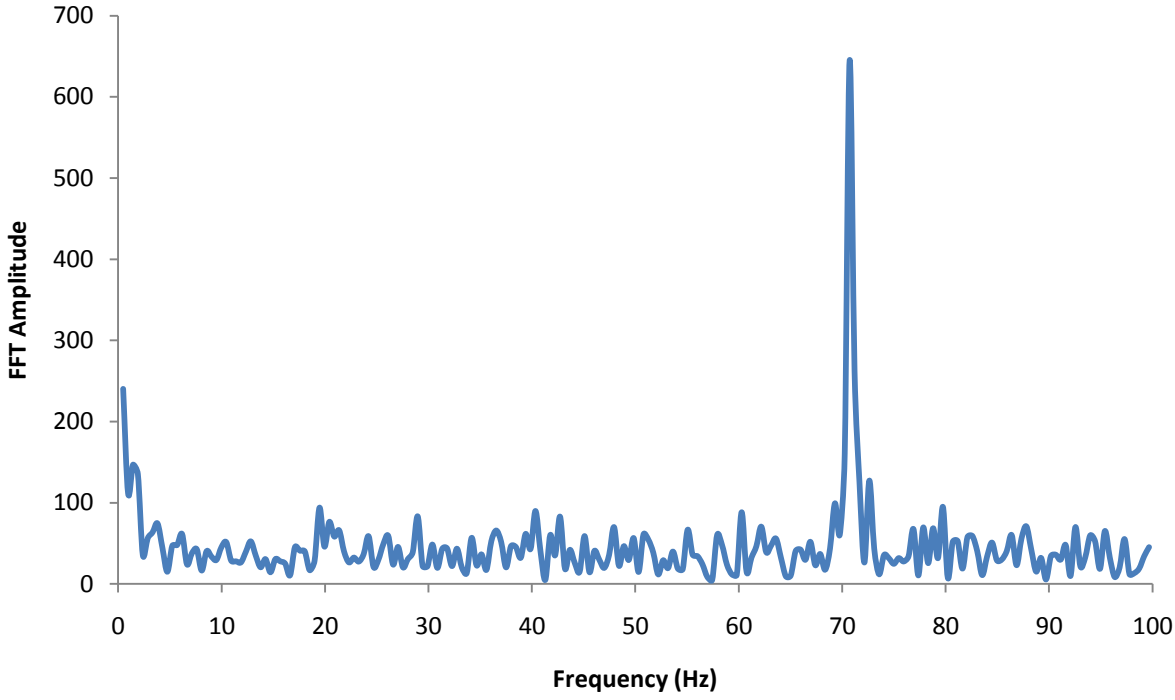

Figure 30: Angular divergence versus time and Fourier spectrum for 23.12g applied mass

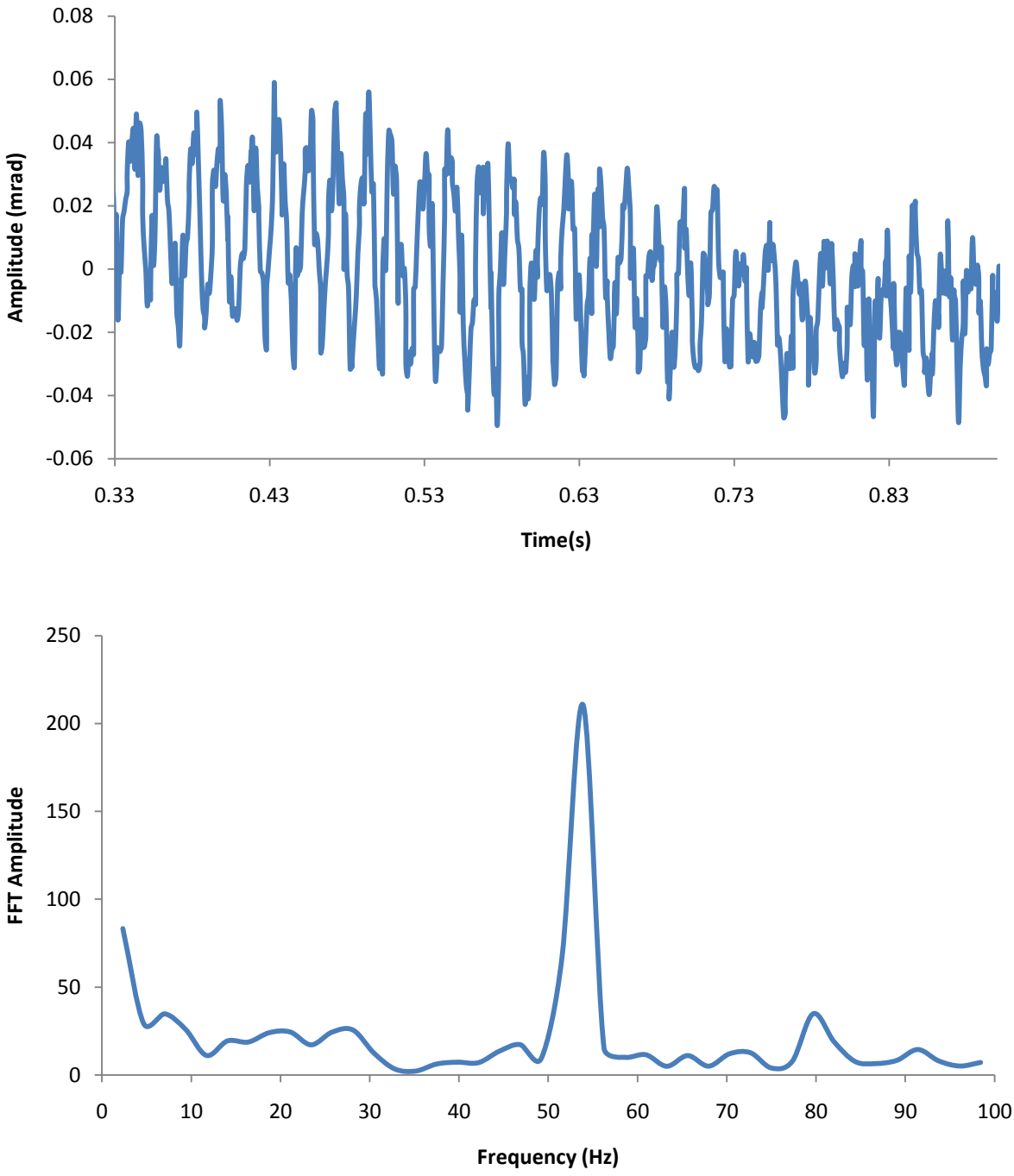

Figure 31: Angular divergence versus time and Fourier spectrum for 17.4g applied mass

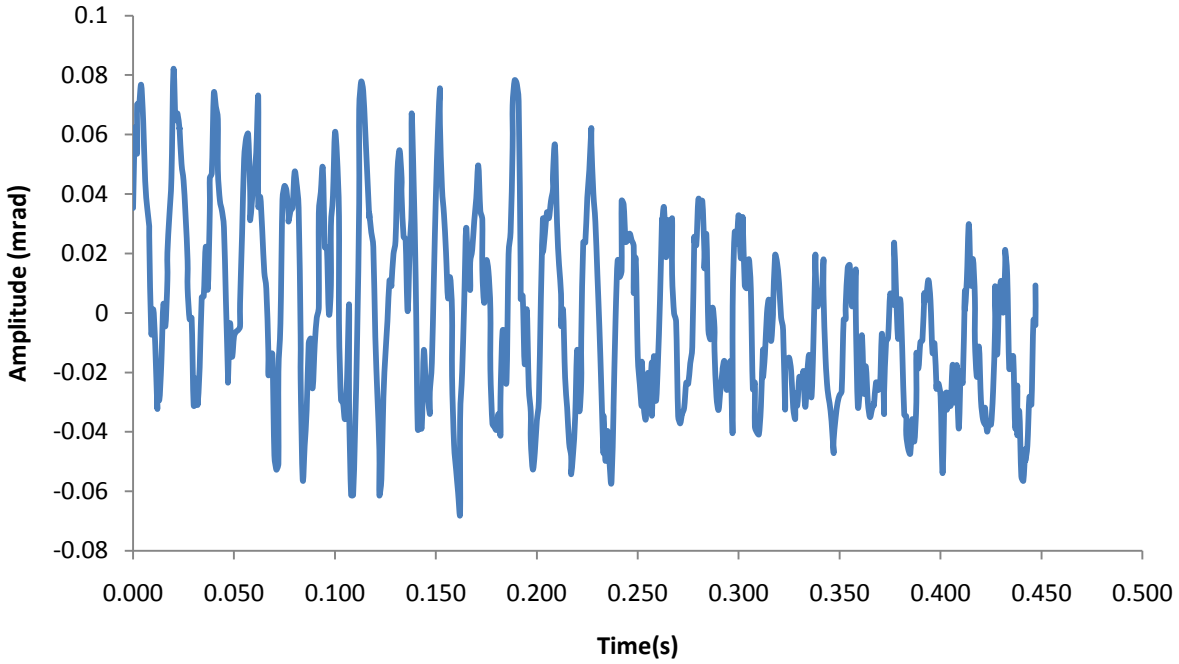

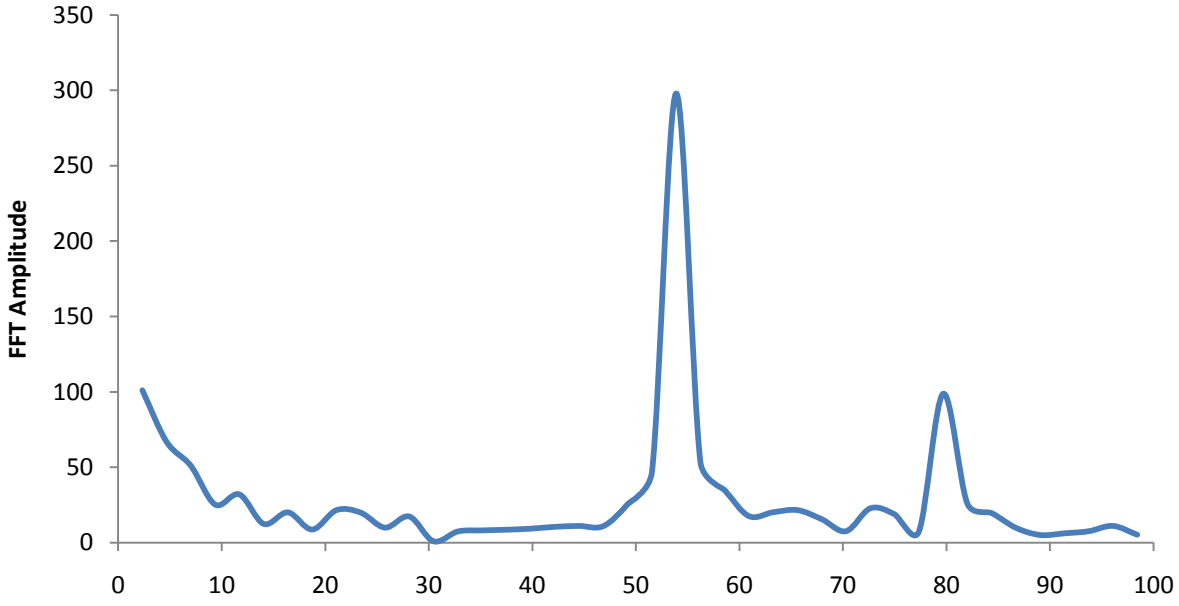

Figure 32: Angular divergence versus time and Fourier spectrum for 11.54g applied mass

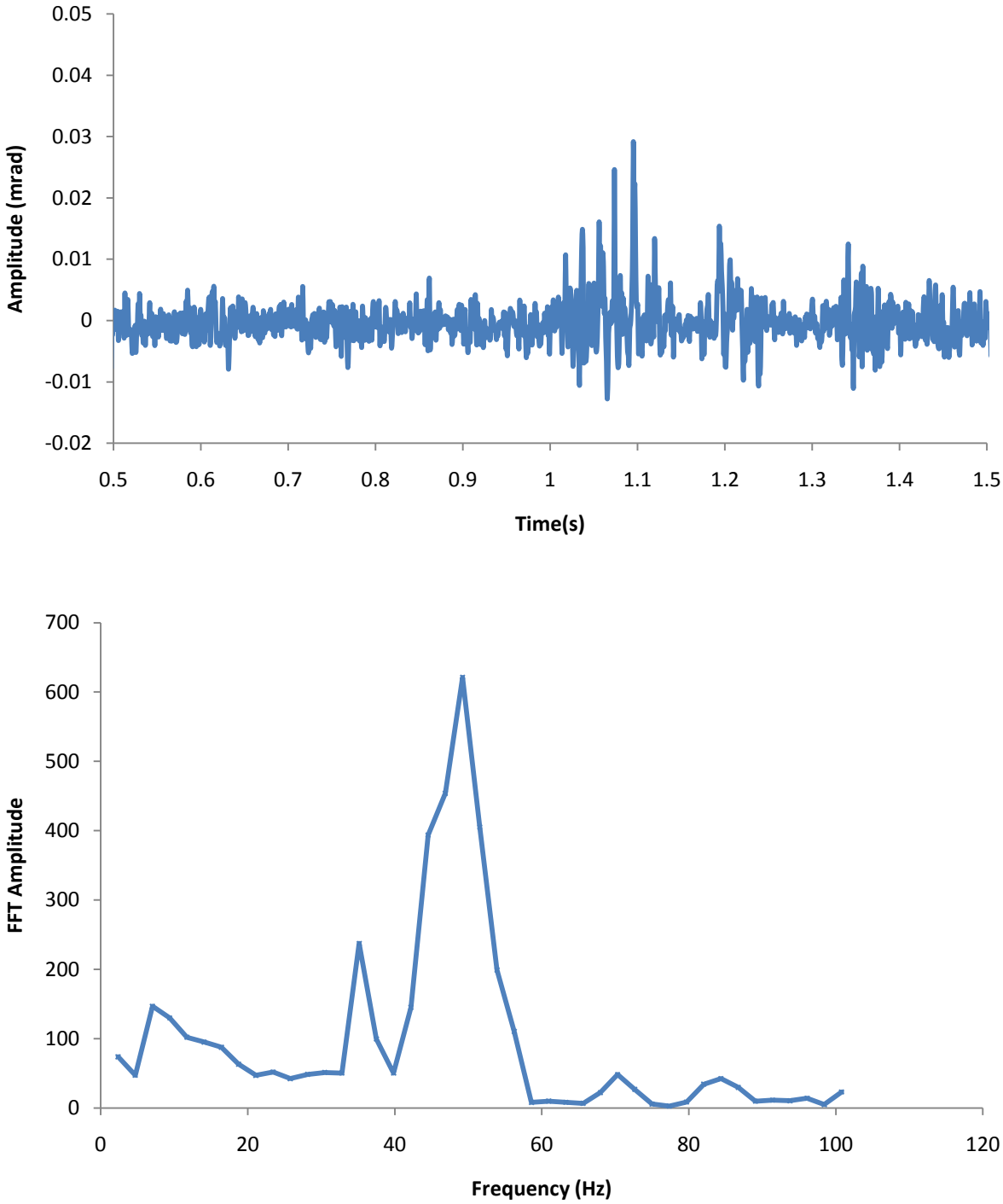

Figure 33: Angular divergence versus time and Fourier spectrum for 5.78g applied mass

Bibliography

[1] The GlueX Collaboration, 2006, GlueX Prosposal. (n.d.). Retrieved from http://dustbunny.physics.indiana.edu/HallD/docs/pac30.pdf

[2] Paton, J., & Isgur, N. (June,1985). Flux-tube Model for Hadrons in QCD. *Physical Review D* , 2910-2929.

[3] Thomson, J. (1897). Cathode Rays. *Philosphical Magazine* , 44.

[4] Rutherford, E. (1911). The scattering of alpha and beta Particles by Matter and the Structure of the Atom. *Philosophical Magazine* , 669-688.

[5] Gell-Mann, M. (1964). A Schematic Model of Baryons and Mesons. *Physics Letters* , 214-215.

[6] Zweig, G. (1964). *An SU(3) Model for Strond Interaction Symmetry and its Breaking.* Geneva: CERN Libraries.

[7] Christman, J. (n.d.). *Color and Charm.* Retrieved from http://35.9.69.219/home/modules/pdf_modules/m283.pdf

[8] Michelson, A. A., & Morley, E. W. (1887). The Relative Motion of the Earth and the Luminiferous Ether. *American Journal of Science* , 333-345.

[9]Chao, A. (1985). *Accelerator Physics in SSC Design.* Berkeley, California.